

Highly potent anti-SARS-CoV-2 multi-DARPin therapeutic candidates

Marcel Walser^{1,*}, Sylvia Rothenberger^{2,3,*}, Daniel L. Hurdiss^{4,5,*}, Anja Schlegel¹, Valérie Calabro¹, Simon Fontaine¹, Denis Villemagne¹, Maria Paladino¹, Tanja Hospodarsch¹, Alexandra Neculcea¹, Andreas Cornelius¹, Patricia Schildknecht¹, Mirela Matzner¹, Martin Hänggi¹, Marco Franchini¹, Yvonne Kaufmann¹, Doris Schaible¹, Iris Schlegel¹, Chloe Iss¹, Thamar Looser¹, Susanne Mangold¹, Christel Herzog¹, Dieter Schiegg¹, Christian Reichen¹, Filip Radom¹, Andreas Bosshart¹, Andreas Lehmann¹, Micha A. Haeuptle¹, Alexander Zürcher¹, Toni Vagt¹, Gabriel Sigrist¹, Marcel Straumann¹, Karl Proba¹, Niina Veitonmäki¹, Keith M. Dawson¹, Christof Zitt¹, Jennifer Mayor^{2,3}, Sarah Ryter², Heyrhyoung Lyoo⁴, Chunyan Wang⁴, Wentao Li⁴, Ieva Drulyte⁶, Wenjuan Du⁴, H. Kaspar Binz⁷, Leon de Waal⁸, Koert J. Stittelaar^{8*}, Sarah Taplin⁹, Seth Lewis¹, Daniel Steiner¹, Frank J.M. van Kuppeveld⁴, Olivier Engler², Berend-Jan Bosch⁴, Michael T. Stumpp^{1,10}, Patrick Amstutz¹

*These authors contributed equally to this work

¹Molecular Partners AG, Wagistrasse 14, 8952 Zurich-Schlieren, Switzerland

²Spiez Laboratory, Austrasse, 3700 Spiez, Switzerland

³Institute of Microbiology, University Hospital Center and University of Lausanne, Rue du Bugnon 48, 1011 Lausanne, Switzerland

⁴Department Biomolecular Health Sciences, Division Infectious Diseases & Immunology - Virology section, Faculty of Veterinary Medicine, Utrecht University, 3584 CL, Utrecht, The Netherlands.

⁵Cryo-Electron Microscopy, Bijvoet Center for Biomolecular Research, Department of Chemistry, Faculty of Science, Utrecht University, Padualaan 8, 3584 CH Utrecht, The Netherlands

⁶Materials and Structural Analysis, Thermo Fisher Scientific, Eindhoven, 5651 GG, The Netherlands.

⁷Binz Biotech Consulting, Lüssirainstrasse 52, 6300 Zug

⁸Viroclinics Xplore, Landerd Campus, Nistelrooise Baan 3, 5374 RE, Schaijk, The Netherlands; ^{8*}

Wageningen Bioveterinary Research, PO Box 65, 8200 AB, Lelystad, the Netherlands

⁹Integrated Biologix GmbH, Steinenvorstadt, 33, Basel, CH-4051, Switzerland.

¹⁰To whom correspondence should be addressed:

Michael T. Stumpp

+41 44 755 77 00

info@molecularpartners.com

Keywords: SARS-CoV-2, COVID-19, corona virus, antiviral therapy, post-exposure prophylaxis, DARPin[®] drug, ankyrin repeat protein, multi-specific, ribosome display

DARPin[®] is a registered trademark owned by Molecular Partners AG

Abstract

Globally accessible therapeutics against SARS-CoV-2 are urgently needed. Here, we report the generation of the first anti-SARS-CoV-2 DARPin molecules with therapeutic potential as well as rapid large-scale production capabilities. Highly potent multi-DARPin molecules with low picomolar virus neutralization efficacies were generated by molecular linkage of three different mono-DARPin molecules. These multi-DARPin molecules target various domains of the SARS-CoV-2 spike protein, thereby limiting possible viral escape. Cryo-EM analysis of individual mono-DARPin molecules provided structural explanations for the mode of action. Analysis of the protective efficacy of one multi-DARPin molecule in a hamster SARS-CoV-2 infection model demonstrated a significant reduction of pathogenesis. Taken together, the multi-DARPin molecules reported here, one of which is currently entering clinical studies, constitute promising therapeutics against the COVID-19 pandemic.

Introduction

Fighting the COVID-19 pandemic will require coordinated global efforts to maximize the benefits of vaccinations and therapeutics(1). Even though vaccine and therapeutic development efforts have progressed considerably, there is, and will be, a remaining medical need for globally accessible therapeutics to treat patients and to protect health care workers, as well as individuals with underlying medical conditions that preclude them from being vaccinated. Neutralizing monoclonal antibodies are expected to be critically important and could be readily available(2-4), however they are complex to manufacture and come at a considerable cost. These logistical hurdles may severely limit accessibility, thus preventing an effective global solution(5).

DARPin molecules are an emerging class of novel therapeutics that are actively being developed in ophthalmology and oncology, with four molecules at a clinical stage(6, 7). Here, we report the generation and characterization of the first anti-viral DARPin molecules in the context of the COVID-19 pandemic. DARPin molecules contain naturally occurring ankyrin repeat motifs. To generate therapeutic DARPin molecules, a pure *in vitro* approach (i.e. selections via ribosome display) is possible and can be carried out in a very short time frame, only requiring the target protein, in this case the SARS-CoV-2 spike protein or subdomains thereof. Hence, therapeutic DARPin molecules can be prepared independently of patient samples or animal immunizations. DARPin molecules can be mono-specific or linked by peptide linkers to form single-chain multi-DARPin molecules with multiple specificities. Notably, DARPin molecules can be manufactured by microbial fermentation, and thus be potentially available world-wide within a short time due to lower technical requirements to provide large-scale clinical grade material. Additionally, the high heat stability of DARPin molecules may offer the prospect of a reduced cold chain for distribution around the globe.

The SARS-CoV-2 spike protein(8, 9), presented as a metastable prefusion trimer at the viral surface, mediates virus entry into the host cell. The spike protein comprises multiple functional domains: S1, which includes the N-terminal domain (NTD) and the receptor binding domain (RBD) responsible for interaction with the angiotensin-converting enzyme 2 (ACE2) host receptor(1, 8, 10, 11), and the S2 domain, which is responsible for virus-host cell membrane fusion via extensive, irreversible conformational changes(12-14). This domain composition opens the possibility to target several sites on a single viral protein, leading to multiple mechanisms of inhibition. Such a multi-pronged approach is expected to lead to higher potencies, lower doses, and better protection against potential viral escape mutations.

With antibody approaches focusing mostly on one or two epitopes of the SARS-CoV-2 spike protein, we present here a novel approach using DARPIn molecules to simultaneously bind three sites on the trimeric SARS-CoV-2 spike protein. The results reported below describe the development and characterization of mono-specific DARPIn molecules against distinct domains of the spike protein, the selection process for the most potent mono-DARPIn molecules and, supported by cryo-EM data, their rational combination into highly potent multi-DARPIn molecules. Furthermore, we demonstrate the protective efficacy of a multi-DARPIn molecule against virus replication and severe disease in a hamster model of COVID-19. We anticipate that antiviral multi-DARPIn molecules have the potential to become an easy-to-deploy antiviral approach for treatment and/or prevention of COVID-19. Based on the results presented here, MP0420 or ensovibep - a derivative of MR-DC, is currently being studied in clinical Phase 1.

Results

Selection and characterization of mono-DARPin molecules targeting different regions of the SARS-CoV-2 spike protein

5 The DARPin technology is based on naïve DARPins libraries(6), with a physical diversity of about 10^{12} different mono-DARPin molecules, allowing the selection of sets of very diverse binding molecules by ribosome display(15, 16), the method of choice when dealing with libraries of such large diversities. DARPins libraries are based on a consensus design approach using hundreds of ankyrin repeat protein sequences of the human and mouse genome(17). An overview of the entire generation process of anti-
10 SARS-CoV-2 spike protein binding DARPin molecules is shown in Figure 1. To obtain individual DARPin molecules binding to distinct domains of the SARS-CoV-2 spike protein and potentially inhibiting viral cell entry, we focused on generating DARPin molecules binding to the receptor binding domain (RBD), the S1 N-terminal domain (NTD) or the S2 domain(18). After four ribosome display selection rounds (Figure 1A), we further enriched for the most potently binding DARPin molecules through screening of
15 3'420 *E. coli* cell extracts overexpressing individual DARPin molecules by homogeneous time-resolved fluorescence (HTRF) assays for binding to different spike protein domains (Figure 1B). Based on binding and ACE2 inhibition profiles obtained in HTRF, which allowed mapping of mono-DARPin molecules to different spike domains, 380 DARPin molecules were selected to be expressed in 96-well format and purified to homogeneity. DARPin molecules were further characterized for antiviral potency in a VSV-
20 pseudovirion neutralization assay (PsV NA) as well as biophysically by size exclusion chromatography (SEC), Sypro-Orange thermal stability assessment(19), ProteOn surface plasmon resonance (SPR) target affinity assessment, and ELISA, to orthogonally evaluate target binding (Figure 1C and D). In parallel to the characterization of the 380 mono-DARPin molecules, 6 mono-DARPin molecules of known spike domain specificity were used to randomly assemble a set of 192 tri-specific DARPin
25 molecules (Figure 1E). The antiviral potencies, determined in a PsV-NA screening assay, of these randomly combined tri-specific DARPin molecules provided valuable information on the most potent tri-specific combinations and formats. Based on the combined data for the 380 mono-DARPin molecules, 11 of them with low pM to low nM affinities, excellent biophysical properties, diversities in amino acid sequences as well as binding for various SARS-CoV-2 spike protein domains (Supplementary
30 Table 1 and Supplementary Figure 1) were selected for the rational generation of 22 multi-DARPin molecules described below (Figure 1F). After detailed characterization of these 22 multi-DARPin candidates, systemic exposure was assessed in mice and in Syrian golden hamsters for the most promising multi-DARPin candidates (Figure 1G). The multi-DARPin candidate with the longer systemic half-life was evaluated for SARS-CoV-2 protection in a Covid-19 Syrian golden hamster model (Figure
35 1H).

Rational design of multi-DARPin molecules targeting the SARS-CoV-2 spike protein

We aimed to increase virus neutralizing potency through molecular linkage of mono-DARPin molecules. Using the 11 selected mono-specific DARPin molecules, a total of 22 multi-DARPin molecules were generated and characterized in detail, each comprising 3 mono-DARPin molecules against various epitopes of the spike protein as well as two mono-DARPin molecules binding to human serum albumin (HSA), which have been previously shown to confer long half-life to other DARPin molecules in animals and humans(7) (Supplementary Table 2). Each of the 22 multi-DARPin molecules contained at least one RBD-binding domain since preventing ACE2 receptor interaction is assumed to be the strongest point of interference with virus entering the host cell. Multi-DARPin molecules were designed to contain several binding modules to RBD (multi-RBD DARPin molecules) or to several distinct domains (multi-mode DARPin molecules). Based on profiling of 22 multi-DARPin molecules for their biophysical properties and antiviral potency (Supplementary Table 2), we selected two multi-DARPin molecules, representative for the two different design strategies (i.e. Multi-RBD-DARPin-Candidate, MR-DC, and Multi-Mode-DARPin-Candidate, MM-DC) for further analysis (Figure 2b). DNA sequencing of the individual mono-DARPin components of MR-DC revealed a similar, but not identical, arrangement of amino acids, suggesting that they share a common mechanism of binding to the RBD. In contrast, the individual components of MM-DC exhibited a high level of sequence diversity, consistent with their different targeting mechanisms (Figure 2c). Neutralization potency for MR-DC and MM-DC was 56 and 36-fold higher in PsV NA, respectively, relative to the most potent neutralizing individual mono-DARPin that was used for the design of the two types of multi-DARPin molecules (Figure 2d-e). In addition, IC₅₀ values for potency determination in a VSV-SARS-CoV2 pseudotype neutralization assay for MR-DC and MM-DC was similar or superior to that of three earlier described potent neutralizing antibodies(20, 21). Neutralization assays with the infectious SARS-CoV-2 yielded IC₅₀ values of 12 pM for MR-DC (1 ng/ml) and 80 pM for MM-DC (7 ng/ml), respectively (Figure 2f). In addition, both multi-DARPin molecules could effectively neutralize pseudotype viruses carrying spike proteins containing natural occurring polymorphisms, including the frequently occurring D614G mutation (Supplementary Table 3). The extremely high neutralization potencies are key for SARS-CoV-2 treatment in particular in a prophylactic setting where very low virus titers at the beginning of the infection are expected.

Cryo-EM analysis of mono-DARPin molecules

To gain further insights into the mode of inhibition and binding, three individual mono-DARPin molecules targeting RBD, S1-NTD, or S2, were subjected to cryo-electron microscopy (cryo-EM) analysis in complex with the trimeric spike ectodomain. In each case, few intact spikes remained

following incubation with the mono-DARPin molecules, particularly with the S2 binder (Supplementary Figure 2). When spike ectodomains were incubated with RBD-binding mono-DARPin molecule #3 for 15 seconds prior to vitrification, 3D classification revealed that 65% of the intact S ectodomains were in the closed conformation, 20% had two RBDs in the open conformation and 15% had all three RBDs in the open conformation (Supplementary Figure 3a). For the open RBD classes, additional density, consistent with the size of a mono-DARPin molecule, was present on the RBD receptor binding ridge (RBR). When the incubation time was increased to 60 seconds, 66% of S ectodomains had three mono-DARPin-bound RBDs in the open conformation (Supplementary Figure 3b). Interestingly, 18% of the S ectodomains had two DARPin-bound RBDs in the open conformation and one trapped in a partially-closed conformation (Supplementary Figures 3b and 4). These results demonstrate that mono-DARPin #3 binding prevents closure of the RBD through a previously described ratcheting mechanism(18). 3D refinement of the fully open class, from the 60 second incubated sample, produced a 6.8 Å global resolution map (Figure 3a and Supplementary Figure 3c-e). The resolution of the map was sufficient to unambiguously assign the pose of RBD-binding mono-DARPin molecule #3, which binds perpendicular to the RBD receptor binding motif (RBM), with its N-terminus orientated toward the spike three-fold symmetry axis (Figure 3a). The concave DARPin binding surface covers the RBR and overlaps with the ACE2 binding site (Figure 3b). Based on the cryo-EM data, molecular docking experiments were performed. The top scoring model indicated that the interface area is ~700 Å² and that key epitope residues are F456, Y473, F486, N487 and Y489, which putatively form an interface of hydrophobic interactions and hydrogen-bonds with the DARPin molecule #3 (Supplementary Figure 5). The proposed model is in line with 30 pM binding affinity measured in SPR. Taken together, these data show that RBD-binding mono-DARPin molecule #3 inhibits SARS-CoV-2 through receptor functional mimicry, facilitating fusogenic conformational rearrangements of the spike protein. This mechanism of inhibition was also observed for a SARS-CoV neutralizing antibody, S230(18), and more recently for a SARS-CoV-2 neutralizing antibody, C105(22). Based on our cryo-EM structure, molecular modelling was used to demonstrate that a linker, used in the multi-DARPin format, would permit simultaneous binding of three RBD-targeting mono-DARPin molecules (Figure 3c).

Following a 15 second incubation with the S1-NTD-binding mono-DARPin molecule #9, 2D classification already revealed clear additional density bound to the spike NTD (Supplementary Figure 2). Subsequent 3D classification revealed that most of the DARPin-bound spikes were in the closed conformation, and 19% had one RBD in open conformation (Supplementary Figure 6a). 3D refinement of the fully closed class produced an 8.8 Å global resolution map (Figure 3d and supplementary Figure 6b-c), sufficient to dock and assign the pose of the bound DARPin molecule (Figure 3d). This mono-DARPin molecule binds to the most distal region of the NTD, which is not resolved in the majority of available spike structures(13, 23). However, several spike structures with nearly completely modelled

NTDs were recently reported(24, 25). The better resolved NTD loops in these structures allowed us to further narrow down the DARPin epitope, indicating that the concave binding surface is ideally situated to interact with the N5 loop, encompassing residues 246-258(26) (Figure 3e). A recently described monoclonal antibody, 4A8(26), also targets the NTD, involving an extensive hydrophilic interaction network with the N3 loop and, to a lesser extent, the N5 loop. In contrast, molecular docking experiments suggest mono-DARPin molecule #9 interacts with the NTD primarily with N5 loop residues 248-252 (Supplementary Figure 7), with an interface area of $\sim 600 \text{ \AA}^2$ and involving both hydrophilic and hydrophobic interactions. Based on our cryo-EM structures, molecular modelling was used to demonstrate that a linker, used in the multi-DARPin format, would permit simultaneous binding of the NTD and RBD-targeting mono-DARPin molecules (Figure 3f).

Cumulatively, our structural analysis allowed us to generate models of the MR-DC and MM-DC molecules in contact with the spike protein using 3D molecular modeling tools (Supplementary Figure 8). In both cases, the half-life extension modules have sufficient space to bind HSA. Within the distance limited by the linker length, we identified a potential binding site for the S2 binder, suggesting that simultaneous binding to the spike protein is feasible. However, structural analysis of S ectodomains incubated with the S2 binder #10 did not reveal any unambiguous density for the bound mono-DARPin. The low number of intact ectodomains remaining after incubation with mono-DARPin #10 suggests that, compared to mono-DARPin molecules #3 and #9, the S2 binder has the greatest destabilizing effect on the structural integrity of the S ectodomains (Supplementary Figure 2).

In vivo antiviral efficacy of a multi-DARPin in a SARS-CoV-2 hamster infection model

In order to assess the *in vivo* antiviral efficacy of our multi-DARPin molecule MR-DC, a hamster Covid-19 disease model was performed to study the potential for preventing SARS-CoV-2 related disease (Figure 4a). Syrian golden hamsters (6 females per group) were treated with a single intraperitoneal dose of one multi-DARPin molecule, MR-DC, using either 16 μg , 160 μg , 1600 μg (per animal; average body weight of $\sim 160\text{g}$), or with placebo, 24 h prior to intranasal infection with SARS-CoV-2. Readouts included observation of macroscopic assessment of tissues, histopathology, body weight and virus titers. Dose-dependent reduction in tissue damage, immune response to infection, body weight loss, virus titers in throat, nasal turbinates and lung tissue was observed, indicating significant anti-viral activity for the 1600 μg dose and a trend for protection for the 160 μg dose under the conditions of the hamster model (Figure 4b-g).

Histopathology results: Intranasal infection with SARS-CoV-2 induced epithelial inflammation and degeneration of the respiratory tract from the nasal turbinates, through the trachea to the bronchi/bronchioles of the lung. More specifically, the inflammation comprised a mixed inflammatory cell infiltrate of lymphocytes, macrophages, plasma cells and granulocytes which was variably

accompanied by epithelial degeneration, regeneration, disorganization, single cell necrosis and inflammatory exudates in the bronchial lumen and nasal cavity. In the lung of more severely affected animals the inflammation extended from the bronchial epithelium to adjacent alveolar interstitium, alveolar sacs and blood vessels (with or without perivascular edema); prominent Type II alveolar pneumocytes and variable hemorrhage were also variably present within the lesion. These findings were most severe in SARS-CoV-2 infected animals receiving the vehicle and the lowest dose of 16ug multi-DARPin MR-DC. While there was some reduction in the severity of the lesion in infected animals given 160 ug, there was a significant improvement in animals treated with the highest dose of 1600 ug (Figure 4b; Supplementary Figure 9).

SARS-CoV-2 infection was accompanied by a reactive change in lymphoid organs consistent with immune activation. Activation of germinal centers was accompanied by increased cellularity of the white pulp in the spleen and increased cellularity of the medullary sinuses (macrophages and plasma cells) in the mandibular lymph node. Again, these findings were generally more apparent in infected animals receiving the vehicle, with a dose-related decrease in severity in MR-DC-treated groups, particularly in animals treated with the highest dose of 1600 ug (Figure 4c; Supplementary Figure 9). The pharmacokinetics for MR-DC, injected at 160 µg and 1600 µg per animal, was evaluated in an independent study in non-infected Syrian golden hamsters, proving systemic exposure for the duration of the in-life phase of this hamster PD model (Supplementary Figure 10).

Discussion

Multiple strategies to combat the COVID-19 pandemic are urgently needed. Next to preventive vaccination approaches, monoclonal antibodies are showing therapeutic promise, based on highly potent virus inhibition and encouraging animal and clinical efficacy(27-29). However, due to the global need for COVID-19, manufacturing is expected to become a major bottleneck for vaccines and antibodies. A number of alternative molecules are being developed to complement and partially overcome this limitation of antibodies. Here we describe the generation of DARPIn molecules - one prominent alternative to antibodies(30) amongst others(31-34) - that bind the SARS-CoV-2 spike protein. We tested a library of one trillion DARPIn molecules and identified multiple DARPIn molecules with different functionalities and binding specificities. By molecular linkage of individual DARPIn molecules, we developed multi-DARPIn molecules with low picomolar neutralizing activity and demonstrated their protective efficacy against SARS-CoV-2 infection in a hamster model. In particular, reduced lung tissue damage and reduced virus replication in the lower and upper respiratory tract were observed, the latter also being important for reducing virus shedding and transmission. The most advanced of those multi-DARPIn molecules, MP0420 or ensovibep, is currently being studied in Phase 1.

The most potent neutralizing mono-DARPIn molecules were found to target the RBD, blocking the spike-ACE2 interaction necessary for infection. This finding is congruent with the identified epitopes of potent neutralizing antibodies obtained from COVID-19 patients(20, 35-39). Thus, the *in vitro* approach using DARPIn molecules independently confirms that the ACE2 interaction site on the SARS-CoV-2 spike protein is one of the most vulnerable sites to block virus infection in cell culture.

The single-chain binding domain nature of DARPIn molecules facilitated the design of multiparatopic and multispecific DARPIn molecules with greatly increased neutralization potencies. Virus neutralization capacity increased substantially when three DARPIn molecules were linked - relative to the individual modules - likely due to both, increased avidity when binding to the trimeric spike proteins as well as multiple spike domains. A similar strategy with comparable outcome has been recently described for nanobodies(31). The observed neutralization capacity of the multi-DARPIn molecules in the low picomolar range is similar to or even outcompetes the neutralizing capacities of monoclonal antibodies. The multi-DARPIn molecules are expected to retain potency even if the spike protein of SARS-CoV-2 should mutate considerably in the future, especially when multiple modes of action are addressed. Evaluation of the impact of a panel of currently reported mutations in the SARS-CoV-2 spike protein revealed no loss of neutralizing capacity of our lead candidates in a PsV NA. Although it remains to be determined if additional mutations will impact the neutralization potencies of the multi-DARPIn molecules, we expect Multi-DARPIn molecules to keep high potency in case the

SARS-CoV-2 spike protein should mutate in the future, especially when multiple domains are addressed.

DARPin molecules(30) have shown good promise for both ophthalmology and oncology patients. Within oncology, MP0250 is the DARPin molecule(7) with most data available to date: MP0250 is a dual inhibitor of VEGF and HGF and is being developed for multiple myeloma in combination with small molecules. MP0250 shows a long systemic half-life of about 2 weeks in human, low immunogenicity potential, and has been given to individual patients for more than two years. All 42 patients in a phase I clinical trial maintained systemic exposure after repeated dosing while 2 patients, out of these 42 patients, showed elevated anti-drug antibodies which did not affect MP0250 exposure. Here, we demonstrate prophylactic protection from SARS-CoV-2 infection by a multi-DARPin molecule in a hamster model. Reported systemic exposures, achieved with human serum albumin binding DARPin molecules, appear comparable to the half-lives reported for monoclonal antibodies. Due to the lack of an immune stimulating Fc-fragment, we envision no generation of antibody dependent enhancement (ADE) effects, a potential additive risk of monoclonal antibodies discussed for patients with inflamed lungs(40-43). Thus, the multi-DARPin molecules represent very attractive potential therapeutics for clinical studies.

Generally, DARPin molecules demonstrate excellent temperature stability and can be easily produced in bacterial expression systems at very high yields allowing cost-effective and scalable production of antiviral biologicals at industrial quantities (supplementary table 5). Consequently, global access to this novel class of therapeutics may be highly additive to monoclonal antibody approaches and thus contribute to overcoming the COVID-19 pandemic(44).

We anticipate that the presented workflow for DARPin development can be applied for any future emerging (corona)virus. We have proven that high-affinity binding and potently neutralizing DARPin molecules can be developed in a matter of weeks, without the requirement of immunization of animals or access to patient materials. Such fast track development strategies of picomolar inhibitors are critical to raise preparedness level towards novel pandemic viruses.

Data availability

The EM density maps for the SARS-CoV-2 spike ectodomain in complex with mono-DARPin #3 (state 1 and state 2), and mono-DARPin #9 have been deposited to the Electron Microscopy Data Bank under the accession codes EMD-11953, EMD-11954 and EMD-11956, respectively. The mono-DARPin and multi-DARPin sequences, and pseudo-atomic models derived from molecular docking experiments, are available (by contacting the corresponding author) for research purposes only under an MTA, which allows the use of the data for non-commercial purposes but not their disclosure to third parties.

Acknowledgements

We would particularly like to thank those colleagues at Molecular Partners who are not included in the author list and are currently advancing the program through the clinic. Additionally, we would like to thank William Lee, former board member of Molecular Partners - and the Virology group at Gilead Sciences for their helpful input. The authors also thank Dr. Gert Zimmer for the gift of the recombinant VSV (Institute of Virology and Immunology (IVI), CH-3147 Mittelhäusern, Switzerland, Department of Infectious Diseases and Pathobiology, Vetsuisse Faculty, University of Bern, CH-3012 Bern, Switzerland). The expression plasmid for the SARS-CoV-2 spike protein was kindly provided by Dr. Giulia Torriani and Dr. Isabella Eckerle (Department of Medicine, University of Geneva, Switzerland). SR & JM were supported by Swiss Federal Office for Civil Protection (Grants Nr. 353008564/Stm, 353008218/Stm, and 353008560/Stm to Olivier Engler and Stefan Kunz).

We would like to thank for the supply of the two 2019-nCoV strains: i) 2019-nCoV/IDF0372/2020 provided by the National Reference Centre for Respiratory Viruses hosted by Institut Pasteur (Paris, France) and headed by Dr. Sylvie van der Werf as well as the human sample from which strain 2019-nCoV/IDF0372/2020 was isolated, provided by Dr. X. Lescure and Pr. Y. Yazdanpanah from the Bichat Hospital.

D.L.H. is funded from by the European Union's Horizon 2020 research and innovation program under the Marie Skłodowska-Curie grant agreement (No 842333) and holds an EMBO non-stipendiary long-term Fellowship (ALTF 1172-2018).

Funding

All studies were funded by Molecular Partners AG, Switzerland.

Author contributions

M.W., S.R., D.L.H., V.C., C.R., S.F., A.Z., N.V., K.M.D., C.Z., M.A.H., L.d.W., K.J.S., F.J.M.v.K., O.E., B.-J. B., M.T.S.; P.A.: conceptualized and designed experiments; M.W., S.R., D.L.H., A.S., D.V., M.P., T.H., A.N., A.C., P.S., M.M., M.H., M.F., Y.K., I.S., C.I., T.L., S.M., C.H., D.S., A.B., A.L., T.V., G.S., K.P., M.S., J.M., S.Ry., S.T., H.L., C.W., W.L., I.D.: performed laboratory experiments; D.L.H., C.R., F.R.: performed computational work; M.W., S.R., D.L.H., H.K.B., S.L., S.F., F.J.M.v.K., O.E., B.-J. B., M.T.S., P.A. drafted the manuscript. S.L., D.S., M.T.S., P.A. acquired funding. All authors reviewed the manuscript.

Competing interests: Molecular Partners authors own performance share units and/or stock of the company. HKB owns stock of the company.

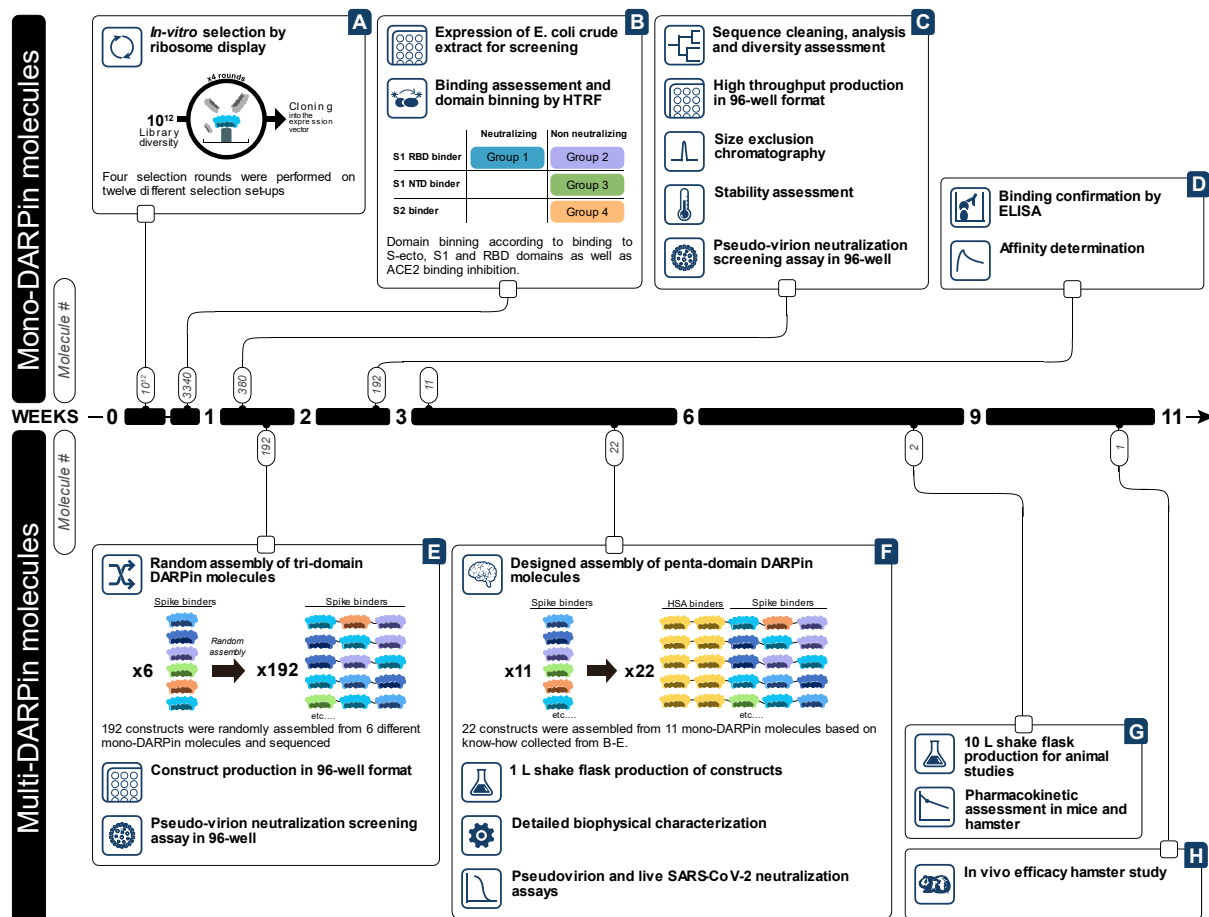


Figure 1: Process overview for the generation of anti-SARS-CoV-2 multi-DARPin molecules. Upper panel, generation and evaluation of mono-DARPin molecules. Lower panel, assembly and deep-characterization of multi-DARPin molecules.

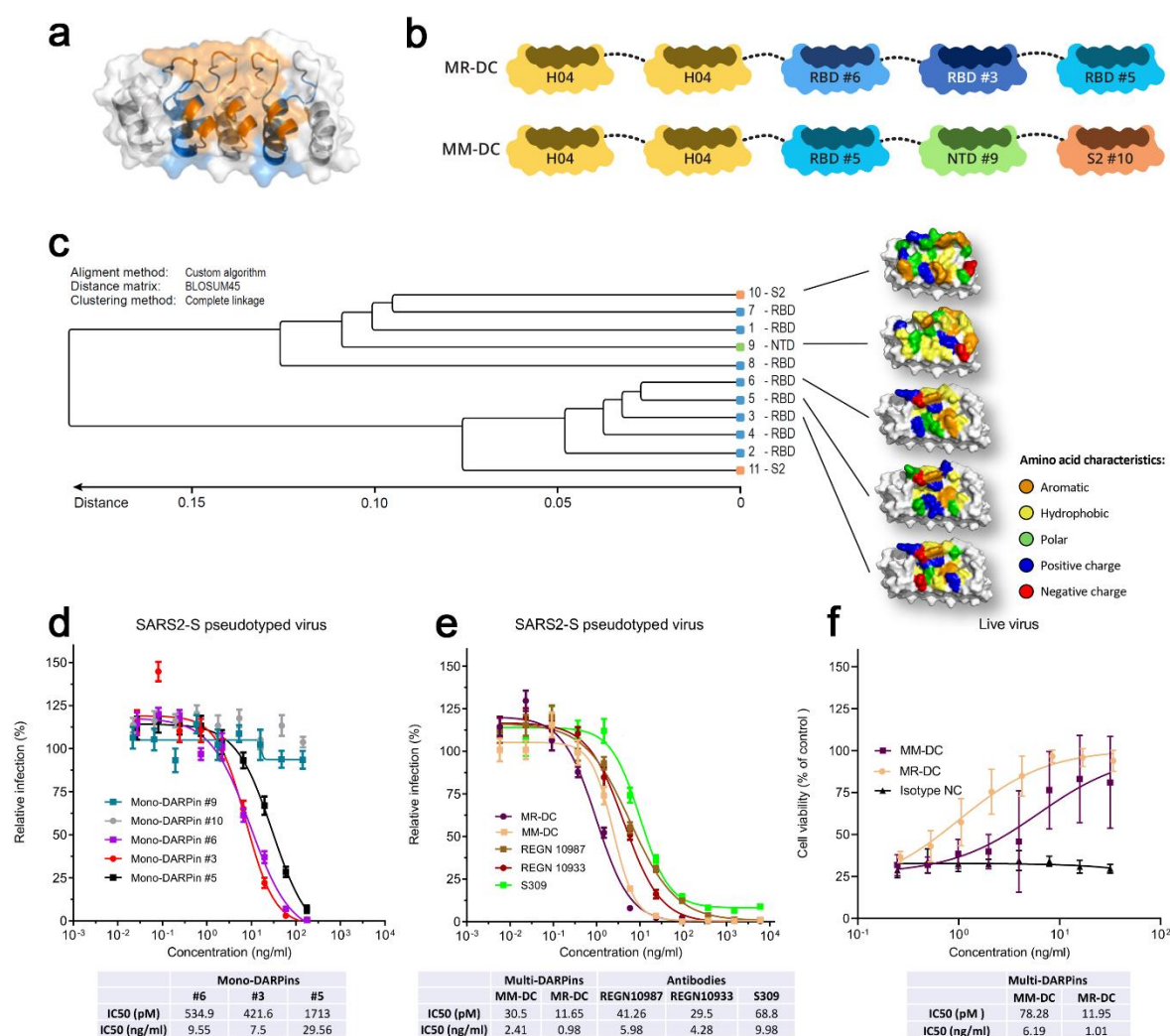


Figure 2: Architecture, diversity and *in vitro* potency of two multi-DARPin molecules. a) Ribbon structure and semi-transparent surface representation of a mono-DARPin molecule. The designed ankyrin repeats are colored alternatingly in white and blue for the five repeats. The randomized residues present in the rigid target binding surface are colored orange. b) Schematic overview of the MR-DC and MM-DC constructs. Protein linkers are depicted as gray dashed lines and the half-life extending human serum albumin binding mono-DARPin (H) is colored yellow. c) Sequence family tree illustrating the sequence diversity amongst the 11 mono-DARPin molecules chosen for the generation of multi-DARPin molecules. Surface representations of five Mono-DARPin molecules binding to the RBD, NTD or S2 are shown, with the amino acid residues in the binding surface colored according to their biophysical characteristics as indicated. d, e) DARPin-respectively antibody-mediated neutralization of infection of luciferase-encoding VSV particles pseudotyped with the SARS-CoV-2 spike protein. Pseudotype VSV particles pre-incubated with mono-DARPin molecules (d), multi-DARPin molecules (MM-DC and MR-DC) or control antibodies (e) at the indicated concentrations were used to infect VeroE6 cells. Luciferase activities in cell lysates were determined at 24 h post transduction to calculate infection (%) relative to mock-treated virus controls. The average ± SD from two independent

experiments performed in sextuplicate is shown. f) Multi-DARPin-mediated cell protection of SARS-CoV-2 infection. SARS-CoV-2 pre-incubated with multi-DARPin molecules MM-DC or MR-DC, or with isotype negative control (isotype NC) at the indicated concentrations were used to infect VeroE6 cells. Cell viability was determined using the CellTiter-Glo luminescent cell viability assay and represented as relative (%) to mock infected cells. Half-maximal inhibitory concentration values (IC_{50}) of DARPin molecules and antibodies are indicated in the lower panel tables (d-f).

5

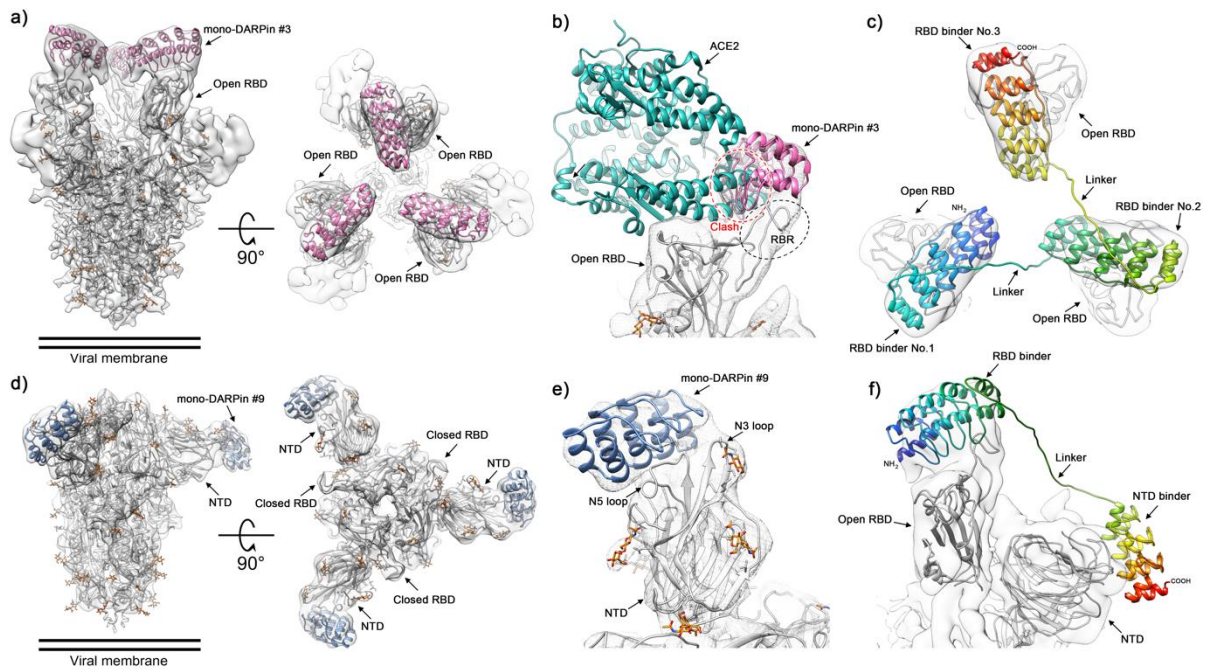


Figure 3: Cryo-EM analysis of mono-DARPin molecules. a) Cryo-EM density for the SARS-CoV-2 spike ectodomain in complex with the RBD targeting mono-DARPin #3, shown as two orthogonal views. The atomic coordinates for the fitted fully open spike (PDB ID: 6XC�) and the DARPin homology model are overlaid and colored grey and pink, respectively. b) Zoomed in view of the DARPin bound RBD with the cryo-EM density shown as a grey mesh. The atomic coordinates of the RBD bound ACE2 (PDB ID: 6M0J), colored green, is superimposed. c) Proposed model of three covalently linked RBD-targeting mono-DARPin molecules shown in a rainbow color scheme from the N terminus (blue) to the C terminus (red). d) Cryo-EM density for the SARS-CoV-2 spike ectodomain in complex with the NTD targeting mono-DARPin #9, shown as two orthogonal views. The atomic coordinates for the fitted fully closed spike (PDB ID: 6ZGE) and the DARPin homology model are overlaid and colored grey and blue, respectively. e) Zoomed in view of the DARPin bound NTD with the cryo-EM density shown as a grey mesh. The N3 and N5 loops are labelled and glycans are shown in stick representation and colored orange. f) Proposed model of the covalently linked NTD and RBD targeting mono-DARPin molecules, shown in a rainbow color scheme from the N terminus (blue) to the C terminus (red).

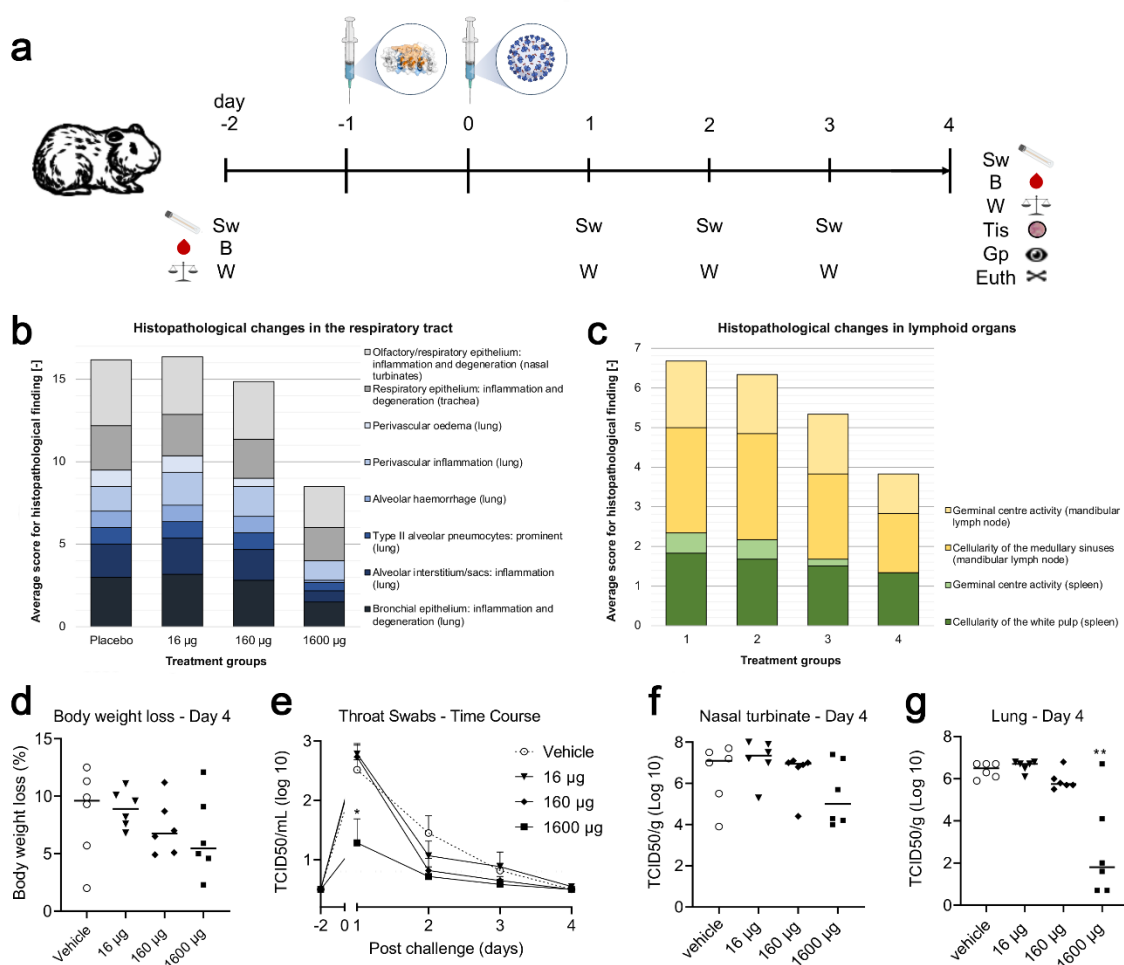


Figure 4: In-vivo efficacy of MR-DC in treating SARS-CoV-2 infection in a preventive Syrian golden hamster model. a) study design: six animals were used per dose group. Generally high variations were observed in control and treatment groups. At Day -2, body weight (W) was measured, blood (B) was taken, and the first throat swab (Sw) performed. Animals were euthanized on Day 4 and tissue (Tis) were taken and gross pathology (Gp) was performed. (b) Histopathological changes in the respiratory tract (lung - blue bars, trachea and nasal turbinates – grey bars). (c) Histopathological changes in lymphoid organs (spleen - green bars, mandibular lymph nodes - yellow bars). A trend to dose-dependent reduction of body-weight loss at day 4 (d), virus titers post challenge for throat swabs (e), nasal turbinate (f) and significant reduction of viral loads in the lung at 1600 µg, with two animals below detection limit, as well as trend to dose-dependent reduction of viral loads at 160 µg (g). Statistically significant differences between Placebo and 1600 µg group: *T-test; P value = 0.0183 / **T-test; P value = 0.0031.

Supplementary Materials for

Highly potent anti-SARS-CoV-2 multi-DARPin

therapeutic candidates

Walser et al.

Materials and Methods

SARS-CoV-2 spike proteins variants used

Proteins used for selections comprised SARS-CoV-2 S protein ectodomain (SARS2-Secto-d72-GCN4-Streptag; University of Utrecht), SARS-CoV-2 S protein (S1+S2 ECT, His-tag; Sinobiological 40589-V08B1), Bio-COVID-19_S1 protein_His_Avitag (Acro Biosystems), SARS2-S1-Flag-3Streptag (University of Utrecht), COVID-19_S_protein_RBD_Fc (Acro Biosystems), and SARS2-S1B-2Streptag (University of Utrecht). Proteins were biotinylated by using standard methods.

Selection of SARS-CoV-2 spike protein-specific DARPins molecules by ribosome display

DARPin libraries(6) (N2C and N3C) were used in ribosome display selections(15, 16) against the SARS-CoV-2 spike protein fragments. Four selection rounds were performed per target and per library using decreasing target concentrations and increasing washing stringency to increase selection pressure from round 1 to round 4. The number of reverse transcription (RT)-PCR cycles after each selection round was continuously reduced, adjusting to the selection yield due to enrichment of binders. The 12 resulting pools were then subjected to a binder screening.

Screening of mono-DARPin molecules

Mono-DARPin molecules specifically binding to the S1-RBD, S1-NTD and S2 domains of the spike protein of SARS-CoV-2 in solution were identified by a homogeneous time resolved fluorescence (HTRF) assay using crude extracts of DARPin-expressing *Escherichia coli* (*E. coli*) cells using standard protocols Briefly, DARPin clones selected by ribosome display were cloned into a derivative of the pQE30 (Qiagen) expression vector, *E. coli* XL1-Blue (Stratagene) was transformed and plated on LB-agar (containing 1% glucose and 50 µg/ml ampicillin) and then incubated overnight at 37°C. Single colonies were picked into individual wells of 96 well plates containing 165 µl growth medium (LB containing 1% glucose and 50 µg/ml ampicillin) and incubated overnight at 37°C, shaking at 800 rpm. 150 µl of fresh LB medium containing 50 µg/ml ampicillin was inoculated with 8.5 µl of the overnight culture in a fresh 96-deep-well plate. After incubation for 120 min at 37°C and 850 rpm, expression was induced with IPTG (0.5 mM final concentration) and continued for 6 h. Cells were harvested by centrifugation of the 96-deep-well plates, supernatant was discarded, and the pellets were frozen at -20°C overnight before resuspension in 8.5 µl B-PERII (Thermo Scientific) and incubation for 1 h at room temperature with shaking (600 rpm). Then, 160 µl PBS was added and cell debris was removed by centrifugation (3220 g for 15 min). The extract of each lysed clone was applied as a 1:200 dilution (final concentration) in PBSTB (PBS supplemented with 0.1% Tween 20® and 0.2% (w/v) BSA, pH 7.4) together with 20 nM (final concentration) biotinylated spike protein domain, 1:400 (final

concentration) of anti-6His-D2 HTRF antibody – FRET acceptor conjugate (Cisbio) and 1:400 (final concentration) of anti-strep-Tb antibody FRET donor conjugate (Cisbio, France) to a well of a 384-well plate and incubated for 120 min at 4°C. The HTRF was read-out on a Tecan M1000 using a 340 nm excitation wavelength and a 620±10 nm emission filter for background fluorescence detection and a 665±10 nm emission filter to detect the fluorescence signal for specific binding. The extract of each lysed clone was tested for binding to the biotinylated spike protein domains, in order to assess specific binding to the spike protein.

Cloning of multi-DARPin molecules

Multi-DARPin molecules were prepared using Gibson assembly as described(45). The individual domains are linked with proline-threonine-rich polypeptide linkers(45).

DARPin protein production and characterization

DARPin molecules were expressed in *E. coli* and purified as described(45). Characterization of mono-DARPin molecules included SDS-PAGE, size exclusion chromatography, surface plasmon resonance, SARS-CoV-2 pseudotype virus inhibition assay, as well as live virus inhibition assay. Characterization of multi-DARPin molecules included SDS-PAGE (fully intact size without degradation; not shown), mass spectrometry (expected molecular weight; not shown), size exclusion chromatography coupled to static light scattering, circular dichroism, storage stability (stable at 60°C for 1 week; data not shown), serum stability (stable at 37°C in serum for one week; data not shown), surface plasmon resonance, SARS-CoV-2 pseudotype virus inhibition assay, live virus inhibition assay, hamster pharmacokinetic analysis, and hamster efficacy model as further described below.

Circular dichroism of DARPin molecules

Circular dichroism measurement was performed with a Jasco J-815 using a 1 cm pathlength cuvette (Hellma) with the monitor sensor inserted in the cuvette. The MRE at 222 nm was followed over a temperature ramp from 20°C to 90°C (heating and cooling). Spectra from 190-250 nm were taken before and after the variable temperature measurement at 20°C. The protein was measured at 0.25 µM in PBS.

Surface plasmon resonance affinity determination of DARPin molecules

SPR assays were used to determine the binding affinity of mono-DARPin as well as multi-DARPin molecules to the spike protein of SARS-CoV-2. All SPR data were generated using a Bio-Rad ProteOn

XPR36 instrument with PBS-T (0.005% Tween20) as running buffer. A new neutravidin sensor chip (NLC) was air-initialized and conditioned according to Bio-Rad manual.

Mono-DARPin molecules: Chemically biotinylated (via lysines) SARS-CoV-2 spike protein 20 (Sino Biologicals) was captured to ~3400 RUs (30 µg/ml, 30 µl/min, 300 s). Two buffer injections (100 µl/min, 60 s) followed by two 12.5 mM NaOH regeneration steps (100 µl/min, 18 s) were applied before the first injections. Mono-domain DARPin proteins were injected (at 50/16.7/5.6/1.9/0.6 nM) for 180 s at 100 µl/min for association and dissociation was recorded for 3600 s (at 100 µl/min). The ligand was regenerated with a 12.5 mM NaOH pulse (100 µl/min, 18 s). The data was double referenced against the empty surface and a buffer injection and fitted according to the 1:1 Langmuir model.

Multi-DARPin molecules: Chemically biotinylated (via lysines) COVID-19_S_protein_RBD_Fc (Acro Biosystems) was captured to ~1000 RUs (775 ng/ml, 30 µl/min, 300 s). Two buffer injections (100 µl/min, 60s) followed by two 12.5 mM NaOH regeneration steps (100 µl/min, 18s) were applied before the first injections. One single concentration of 25 nM of each multi- domain drug candidate was injected for 180 s at 100 µl/min for association and dissociation was recorded for 36'000 s (at 100 µl/min). The data was double referenced against the empty surface and a buffer injection. Due to avidity gain, no significant dissociation could be recorded during the measured time.

Cells and viruses

Vero E6 cells (African green monkey kidney cells, ATCC® CRL1586™) purchased from ATCC (Manassas, VA 20110 USA) were passaged in cell culture medium DMEM (FG0445) containing 10% FBS and supplements (2mM L-Glutamine, Non-essential amino acids and 100 U/ml Penicillin 100 µg/ml Streptomycin and HEPES, all from Biochrom, Berlin, Germany) at 37°C with CO₂. SARS-CoV-2 (2019-nCoV/IDF0372/2020) kindly provided by Dr. Sylvie van der Werf from the National Reference Centre for Respiratory Viruses hosted by Institut Pasteur (Paris, France) was propagated in Vero E6 cells in MEM containing 2% FBS and supplements (2%-FBS-MEM) at 37°C and 5% CO₂.

Virus neutralization capacity of mono-DARPin and multi-DARPin molecules was determined for 100 TCID₅₀ SARS-CoV-2 by crystal violet staining of protected cells. DARPin molecules were serially diluted from 50 nM to 3.2 pM (in triplicates) in 100 µl cell culture medium (2%-FBS-MEM) enriched with 10 µM human serum albumin (HSA, CSL Behring, Switzerland) (2%-FBS-MEM + HSA) in 96 well plates. The diluted DARPin candidates were exposed to 100 TCID₅₀ SARS-CoV-2 (10⁴ TCID₅₀/ml) in 100 µl 2%-FBS-MEM + HSA. DARPin/virus mixtures (200 µl) were transferred onto 80% confluent Vero E6 cells. The controls consisted of Vero E6 cells exposed to DARPin molecules only, to determine unspecific effects of the DARPin molecules, of cells exposed to virus suspension only to determine maximal cytopathic effect and of cells incubated with medium only, to determine baseline state of cells. The plates were

incubated for 3 days at 37°C and the cytopathic effect determined by staining with 100 µl/well crystal violet solution (spatula tip (~4 mg) crystal violet powder (Sigma Aldrich) solved in 30 ml 37% formalin and 120 ml PBS (Sigma Aldrich)) for 10 min and washing plates with PBS (Sigma Aldrich). Wells were visually evaluated for complete protection indicated by intact blue/violet cell layer or partial protection in case of >50% intact cell layer.

The effect of neutralization capacity of Multi-DARPin was evaluated by exposing serial dilutions of the DARPin candidates to increasing titers of SARS-CoV-2 and determining cell protection by CellTiter-Glo assay (Promega, Madison, USA). Serial dilution of DARPin candidates were prepared in 96 well plates in 100 µl cell culture medium (2%-FBS-MEM + HSA) mixed with 100 µl virus suspension of 10⁴ TCID₅₀/ml SARS-CoV-2 and incubated for 1 h at 37°C and 5% CO₂. DARPin/virus mixtures (200 µl) were transferred onto 80% confluent Vero E6 cells and plates incubated at 37°C for 3 days. Cell viability was determined by removing 100 µl supernatant from all wells and adding 100 µl CellTiter-Glo reagent as described in the manufacturers protocol (CellTiter-Glo® Luminescent Cell Viability Assay). Luminescence was read after 2 minutes shaking on an orbital shaker and 10 min incubation at RT using the GloMax instrument (Promega, Madison, USA).

SARS-CoV-2 VSV pseudotype virus assay

SARS-CoV-2 pseudoviruses were generated as described previously(46). A selected panel of 380 DARPin molecules expressed in 96-well format and purified to homogeneity were evaluated for their anti-viral activity in a pseudovirus screening assay. In parallel, 6 mono-DARPin molecules of known spike domain specificity which were randomly assembled in a set of 192 tri-specific DARPin molecules were included in the screen. For the pseudovirus screening assays, DARPin molecules were diluted in Dulbecco modified Eagle medium (DMEM)-2 % [vol/vol] fetal calf serum (FCS) at the following concentrations: 200 nM, 20 nM, 2nM and 0.2 nM and mixed with an equal volume of DMEM-2 % [vol/vol] FCS containing the VSV-based SARS-CoV-2 pseudoviruses to obtain 2000 IU/well. The mix was incubated for 60 min at 37°C, then inoculated onto Vero E6 cells in a clear bottom white walled 96-well plate during 90 min at 37°C. The inoculum was removed and fresh medium added, and cells further incubated at 37°C for 16 h. Cell were lysed according to the ONE-Glo™ luciferase assay system (Promega, Madison, US) and light emission was recorded using a Berthold® TriStar LB941 luminometer. For the pseudovirus titrations an initial dilution of the drug was followed by two-fold dilutions in quadruplicates in DMEM)-2 % [vol/vol] FCS supplemented with 20 µM human serum albumin (CSL Behring). The mixture was mixed with an equal volume of DMEM-2 % FCS containing SARS-CoV-2 pseudoviruses and incubated for 90 min at 37°C. Neutralizations were performed from 200 to 2000 infectious units (IU) per well, depending on the experiment. Following this incubation,

the mix was inoculated onto Vero E6 cells in a clear bottom white walled 96-well plate during 90 min at 37°C. The inoculum was removed and fresh medium added, and cells further incubated at 37°C for 16 h. Cells were lysed according to the ONE-Glo™ Luciferase assay system (Promega, Madison, US) and light emission was recorded using a Berthold® TriStar LB941 luminometer. The raw data (relative light unit values) were exported to GraphPad Prism v8.01, and the % neutralization data were normalized to the untreated PsV signal. IC₅₀ with 95% confidence interval were estimated by model of nonlinear regression fit with settings for log (inhibitor) vs normalized response curves.

Laboratory 2: PsV NA for titration curves

Production of VSV pseudotyped with SARS2-S was described previously(47). Briefly, HEK-293T cells were transfected with pCAGGS expression vectors encoding MERS-S, SARS-S or SARS2-S carrying a 16-, 28- or 18-a.a. cytoplasmic tail truncation, respectively. One day post transfection, cells were infected with the VSV-G pseudotyped VSVΔG bearing the firefly (*Photinus pyralis*) luciferase reporter gene. Twenty-four hours later, supernatants containing SARS2-S pseudotyped VSV particles were harvested and titrated on African green monkey kidney Vero E6 (ATCC#CRL-1586) cells.

In the virus neutralization assay, DARPins were threefold serially diluted at two times the desired final concentration in DMEM supplemented with 10 μM human serum albumin (CSL Behring), 100 U/ml Penicillin and 100 μg/ml Streptomycin (Lonza). Monoclonal antibodies against MERS-S (2), SARS-S or SARS2-S were included as a positive control(47). Diluted DARPins and mAbs were incubated with an equal volume of pseudotyped VSV particles for 1 hour at room temperature, inoculated on confluent Vero E6 monolayers in 96-well plate, and further incubated at 37 °C for 24 hours. Cells were lysed with Luciferase Cell Culture Lysis 5X Reagent (Promega) at room temperature for 30 min. Luciferase activity was measured on a Berthold Centro LB 960 plate luminometer using D-luciferin as a substrate (Promega). The half maximal inhibitory concentrations (IC₅₀) were determined using 4-parameter logistic regression (GraphPad Prism version 8).

Cryo-electron microscopy

4 μl of purified S ectodomain (9 μM) was mixed with 1 μl of 50 μM mono-DARPins #3, #9 or #10, and incubated for 15 seconds at room temperature. 3 μl of sample was then dispensed on Quantifoil R1.2/1.3 200-mesh grids (Quantifoil Micro Tools GmbH) that had been freshly glow discharged for 30 s at 20 mA. Grids were blotted using blot force +2, for 5 s using Whatman No. 1 filter paper and immediately plunge-frozen into liquid ethane cooled by liquid nitrogen using a Vitrobot Mark IV plunger (Thermo Fisher Scientific) equilibrated to ~95% relative humidity, 4°C. Movies of frozen-hydrated specimens were collected using Glacios Cryo-TEM (Thermo Fisher Scientific) operating at 200 keV and equipped with a Falcon 4 Direct Electron Detector (Thermo Fisher Scientific). For

additional analysis of mono-DARPin #3, 4 μ l of purified S ectodomain (18 μ M) was mixed with 1 μ l of 100 μ M DARPin, and incubated for 60 s at room temperature. Grids were prepared as described above, and movies were collected using a Titan Krios Cryo-TEM (Thermo Fisher Scientific) operating at 300 keV and equipped with a Falcon 4 Direct Electron Detector (Thermo Fisher Scientific). All cryo-EM data were acquired using the EPU 2 software (Thermo Fisher Scientific) with a 30-degree stage tilt to account for preferred orientation of the samples. Movies were collected in electron counting mode at 92,000x (Glacios) or 75,000x (Titan Krios), corresponding to a pixel size of 1.1 Å/pix over a defocus range of -1.25 to -2.5 μ m.

Image processing

Movie stacks were manually inspected and then imported in Relion version 3.0.1(48). Drift and gain correction were performed with MotionCor2(49), and GCTF(50) was used to estimate the contrast transfer function for each movie. Particles were automatically picked using a gaussian blob template and Fourier binned (2 x 2) particles were extracted and subjected to two rounds of 2D classification, ignoring CTFs until the first peak. Particles selected from 2D classification were subject to a single round of 3D classification. Particles belonging to the best classes were re-extracted unbinned, 3D auto-refined and post-processed. Iterative rounds of per particle defocus estimation, 3D auto-refinement and post-processing were used to account for the 30-degree stage tilt used during data collection. An overview of the image processing workflows for each of the mono-DARPin samples is shown in supplementary Figure 2.

Molecular modeling of mono and multi-DARPin molecules

Homology models of mono-DARPin molecules #3 and #9 were generated with Rosetta(51). The consensus designed ankyrin repeat domain PDB ID:2xee was used as template. Mutations were introduced with RosettaRemodel(52) with fixed backbone, and the structure was refined with RosettaRelax(53). Forty refined structures were clustered using RosettaCluster with 0.3 Å radius, and the lowest-energy model from the largest cluster served as the final model. These models were then used for fitting domain #3 and #9 into the observed electron density generated from the complex structure of the spike protein.

To facilitate accurate fitting of the DARPin coordinates into their respective cryo-EM maps, difference density maps of the bound DARPin molecules were produced as described previously(54). For mono-DARPin #3, the atomic coordinates of a fully-open spike ectodomain (PDB ID: 6XC�) were fitted into the EM density using the UCSF Chimera ‘fit in map’ tool. The Fab component of the model was deleted, and then the ‘molmap’ command was used to simulate a 7 Å resolution density map. This simulated

map was then resampled on the grid of the experimental cryo-EM density map using the ‘vop resample’ command. The ‘vop subtract’ command was then used to subtract the value of the simulated map from the experimental map. The ‘minRMS’ option was used to automatically scale the simulated map to minimize the root-mean-square sum of the resulting subtracted values at grid points within the lowest contour of simulated map. The UCSF Chimera ‘fit in map’ tool was then used to fit mono-DARPin #3 into the difference density until the correlation between the map and model did not improve any further, and ensuring that the epitope binding surface of the mono-DARPin was orientated towards the spike ectodomain. This workflow was then repeated for mono-DARPin #9, using the fully closed spike coordinates (PDB ID: 6ZGE).

The PDB file with the coordinates of the trimer of domain #3:RBD was used as an input structure for the conceptual modeling of MR-DC bound to the spike ectodomain as shown in Supplementary Figure 8. In both models, the open RBD domain from PDB ID 6vyb was used to generate three RBDs in the open conformation(13). For the conceptual modeling of MM-DC a similar approach was used by fitting domain #9 into the observed density of the NTD cryo-EM structure. Additionally, a structurally resolved NTD domain from PDB 7c2l was used(26), and a binding domain model of S2 (#10) was placed manually to a potential interacting site on S2 (non-glycosylated region within reasonable distance from the binding domain #9, based on linker length). For both structures, HSA binding DARPin models were placed and the linkers between each binding domain were modeled using Rosetta modeling tools(52).

In a last step, the models of mono-DARPin #3:RBD (residues 303-526) and mono-DARPin #9:NTD (residues 14-303) were refined with Rosetta. The structures were pre-relaxed for docking and served as input for local, high-resolution docking with RosettaDock(55) with fixed backbone. Five hundred models were generated and clustered with 1 Å radius (RosettaCluster). Two largest clusters were inspected and the lowest-energy model from more conserved group (i.e., with lower rigid-body perturbation from the input structure) was taken further for additional all-atom refinement with RosettaRelax(53), with protocol optimized for interfaces (InterfaceRelax2019). Fifty models were generated, and the lowest scoring model was selected. This model was used to describe the interactions between DARPin molecules and their target domains. Figures were generated using LigPlot(56), UCSF Chimera(57), PyMOL (The PyMOL Molecular Graphics System, Version 2.0, Schrödinger, LLC) and BioRender (BioRender.com).

Prophylactic Syrian golden hamster model for the assessment of antiviral potency of candidate MR-DC

The study was performed at Viroclinics Xplore, Schaijk, The Netherlands.

Virus used for Syrian golden hamster study

SARS-CoV-2 isolate BetaCoV/Munich/BavPat1/2020 was kindly provided by Prof. Dr. C. Drosten (European Virus Archive Global # 026V-03883). With a history of 1 passage in Vero-TMPRSS2 and 3 passages in Vero E6 cells (ATCC), the seed stock was titrated in Vero E6 cells to a concentration of 7.1 log₁₀ TCID₅₀/ml. The seed stock was thawed and diluted in cold phosphate-buffered saline (PBS) prior to infection.

Experimental design

Twenty-four specific-pathogen-free (SPF) 15 weeks-old Syrian golden hamsters (*Mesocricetus auratus*, females and males, approximate body weights of 160g, provided by Envigo) were uniquely identified using individually-coded animal markers. They were housed in elongated type 2 group cages with two animals per cage under BSL-III conditions during the experiment. They were kept according to the standards of Dutch law for animal experimentation and were checked daily for overt signs of disease. The study was carried out following approval by an independent animal welfare body (approval AVD277002015283-WP13) and complied with all relevant ethical regulations for animal testing.

Four groups of six hamsters were treated with multi-DARPin molecule MR-DC via the intraperitoneal route with 16 µg, 160 µg, or 1600 µg doses per animal or with a placebo 24 hours prior to infection and subsequently animals were inoculated intra-nasally with 100 µL PBS containing 5x10⁴ TCID₅₀ SARS-CoV-2. The inoculum was instilled dropwise using a pipette and equally divided over both nostrils. The animals were weighed regularly and throat swabs, for quantitative PCR and infectious virus titration, were collected on a daily basis. For all animal procedures, the animals were sedated with isoflurane (3-4%/O₂).

Upon necropsy at day 4 post infection, full-body gross pathology was performed for each animal and all abnormalities recorded and described. All lung lobes were inspected, and the percentage of affected lung tissue was estimated by eye. Samples of the left nasal turbinates, trachea and the entire left lung (often with presence of the primary bronchi) were preserved in 10% neutral buffered formalin for histopathology. Samples of the right lung parenchyma and right nasal turbinates were frozen for quantitative PCR and virus titration.

Virology

Throat swabs and homogenized tissue samples (lungs and nasal turbinates) were thawed and tested for the presence of SARS-CoV-2 infectious virus using virus titration. To this end, quadruplicate 10-fold serial dilutions were used to determine the virus titers on confluent layers of Vero E6 cells. Serial

dilutions of the samples (throat swabs and tissue homogenates) were prepared and incubated on Vero E6 monolayers for 1 hour at 37°C. Vero E6 monolayers were washed and incubated with infection medium for 4-6 days at 37°C after which plates were scored for cytopathogenic effect (CPE) using the vitality marker WST-8. Viral titers (TCID₅₀) were calculated using the method of Spearman-Kärber.

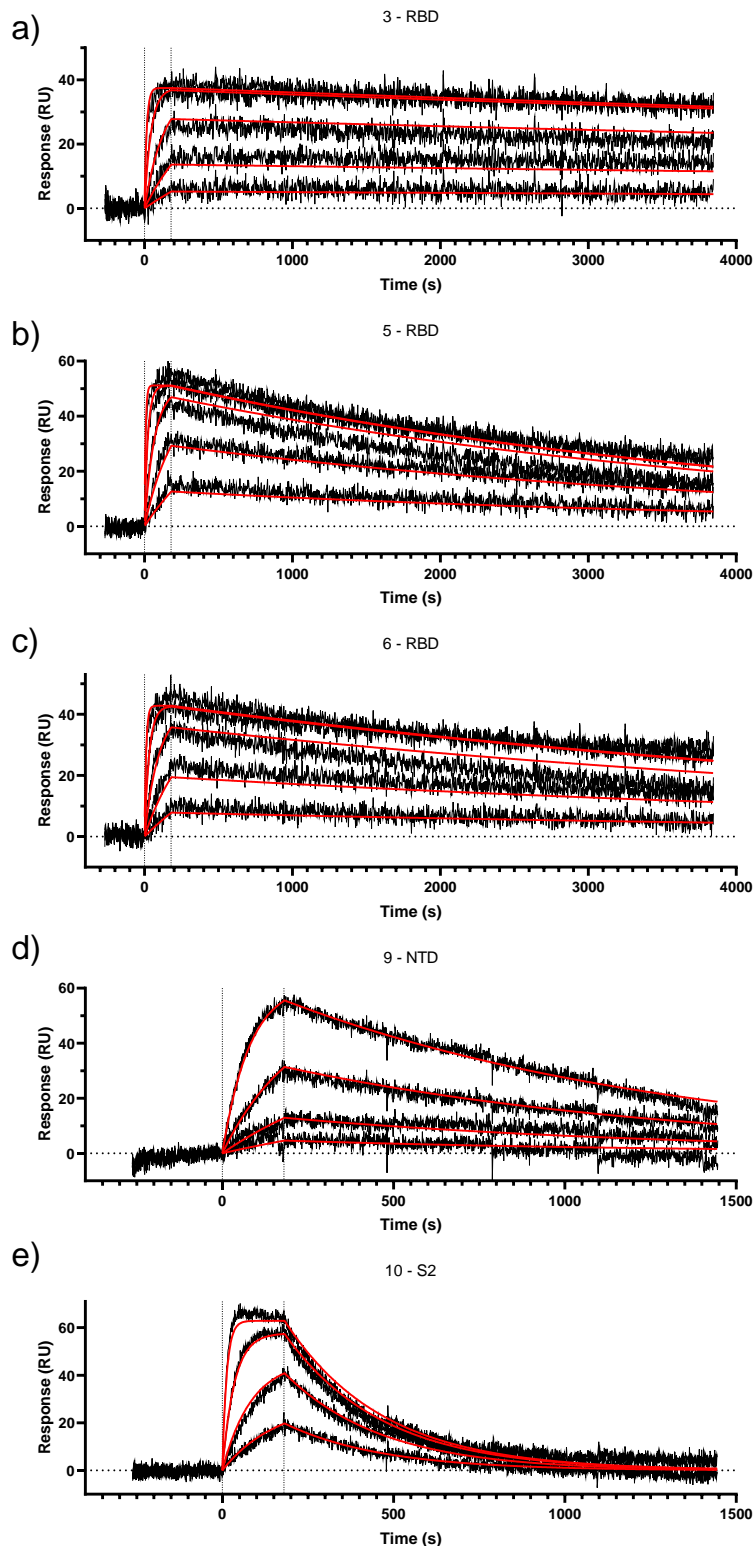
Histopathology

Samples of tissue from the respiratory tract (lung, trachea, and nasal turbinates) and lymphoid organs (spleen and mandibular lymph node) were fixed in 10% neutral buffered formalin (24-48h) and embedded in paraffin. Tissue sections were then stained with hematoxylin and eosin and examined by light microscopy. A semi-quantitative histopathological analysis was performed, and findings scored using the following grades: absent (grade 0), minimal (grade 1), mild (grade 2), moderate (grade 3) or marked (grade 4). The average score for the dose groups was calculated for each finding in the respiratory tract (Figure 4b) and lymphoid organs (Figure 4c).

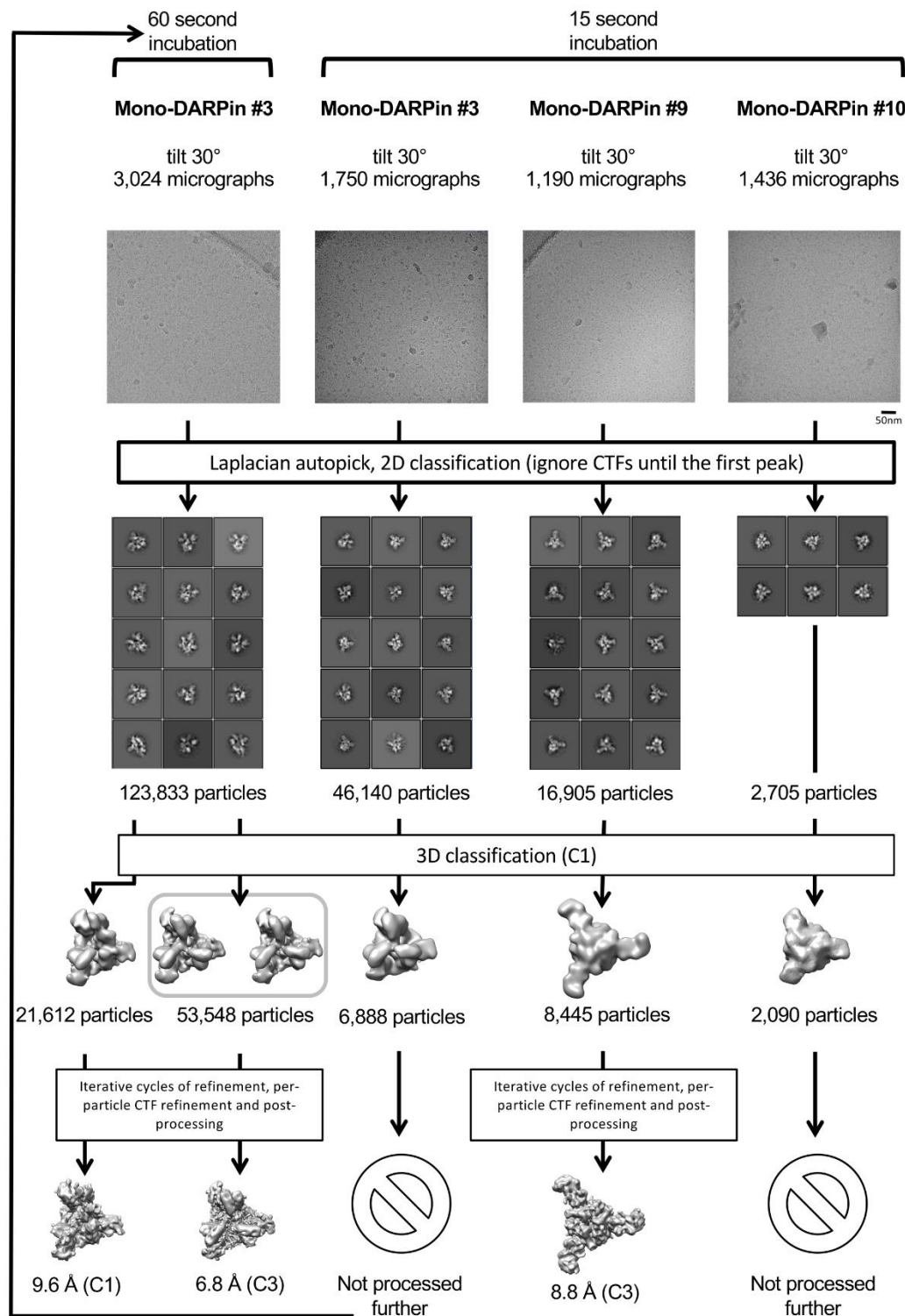
Hamster pharmacokinetic study

Single-dose intraperitoneally administered dose pharmacokinetic measurements in female hamsters (n = 6 per group) were performed at 1 mg/kg and 10 mg/kg. Blood samples were collected pre-dose and again at 1 h, 4 h, 8h, 12h, 24 h, 48 h, 72 h, 96 h and 168 h post-injection. Serum concentrations were determined by sandwich ELISA using RBD as capture reagent and an anti-His-tag antibody as detection reagent and using a standard curve. Pharmacokinetic parameters were determined using the software Phoenix WinNonLin (Certara, Princeton, USA) or GraphPadPrism (GraphPad Software, La Jolla, USA) and non-compartmental analyses.

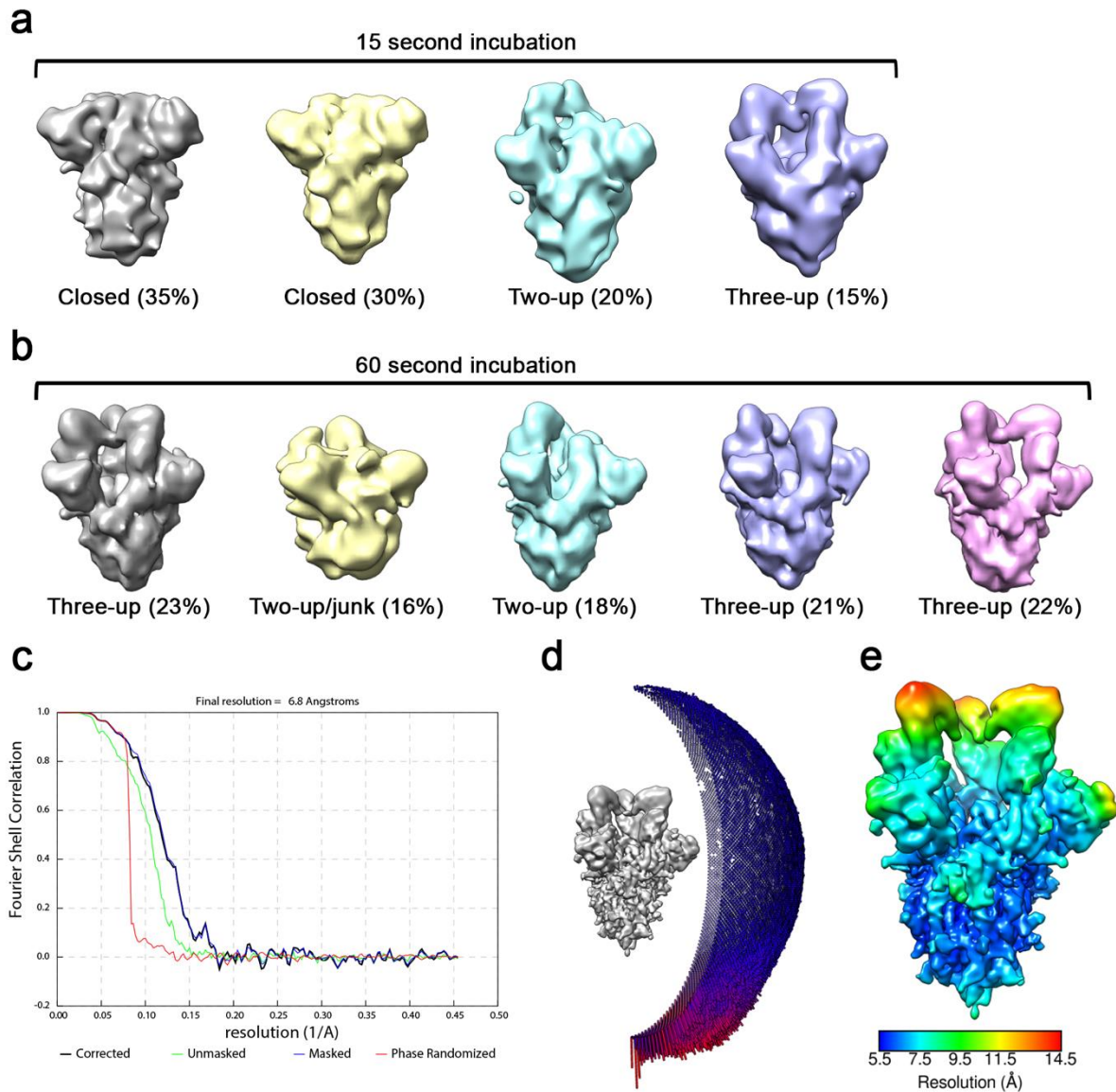
Supplementary Figures



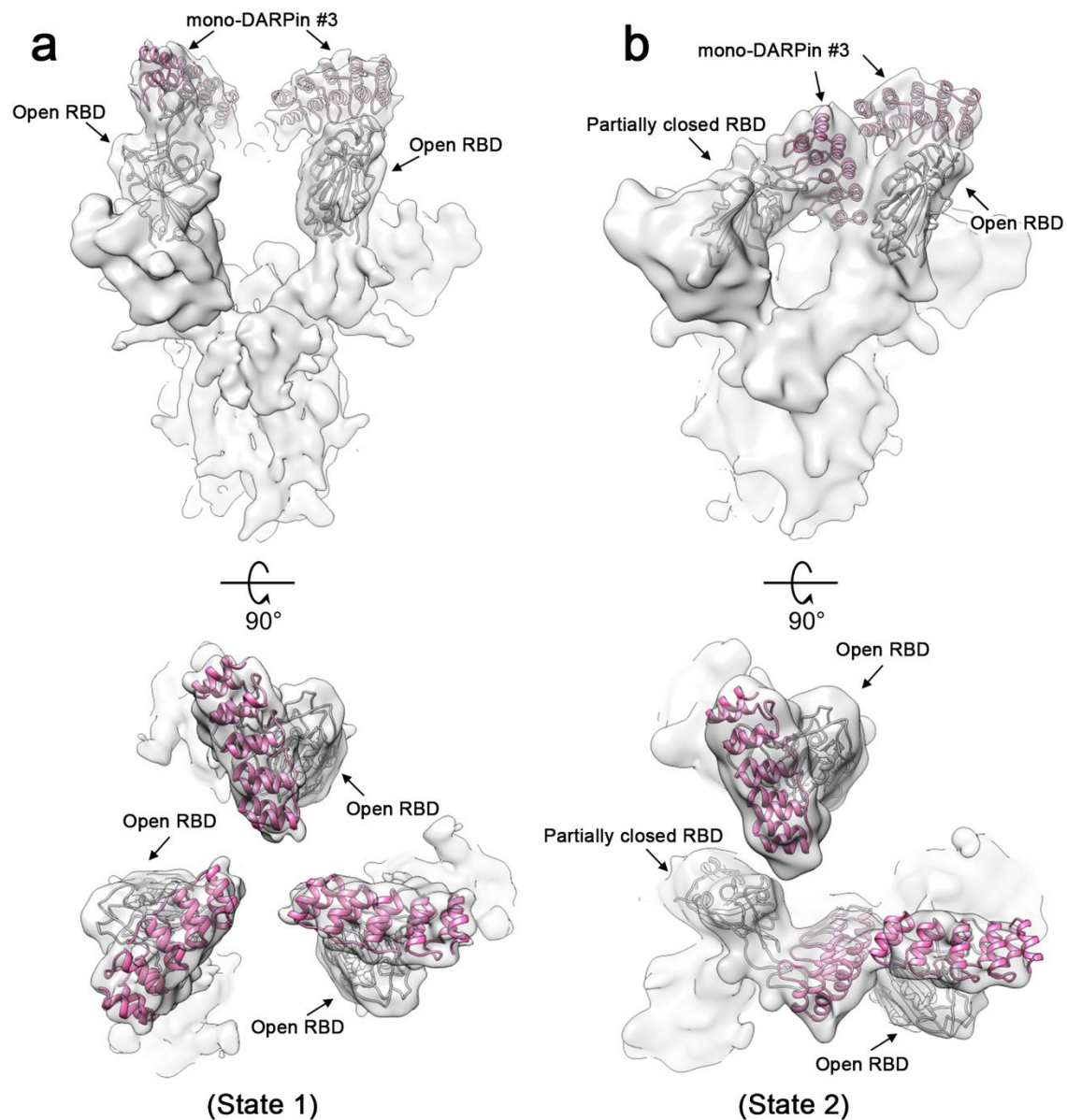
Supplementary Figure 1: Surface plasmon resonance (SPR) sensorgrams of the mono-DARPin molecules #3 (a), #5 (b), #6 (c), #9 (d), #10 (e), incorporated in MR-DC (a-c) and MM-DC (c-e) binding to immobilized trimeric spike protein. DARPin concentrations for a-c: 50/16.67/5.56/1.85/0.62 nM. DARPin concentrations for (d) and (e): 16.67/5.56/1.85/0.62 nM. Affinity values of mono-DARPin molecules are listed in **Table 1**.



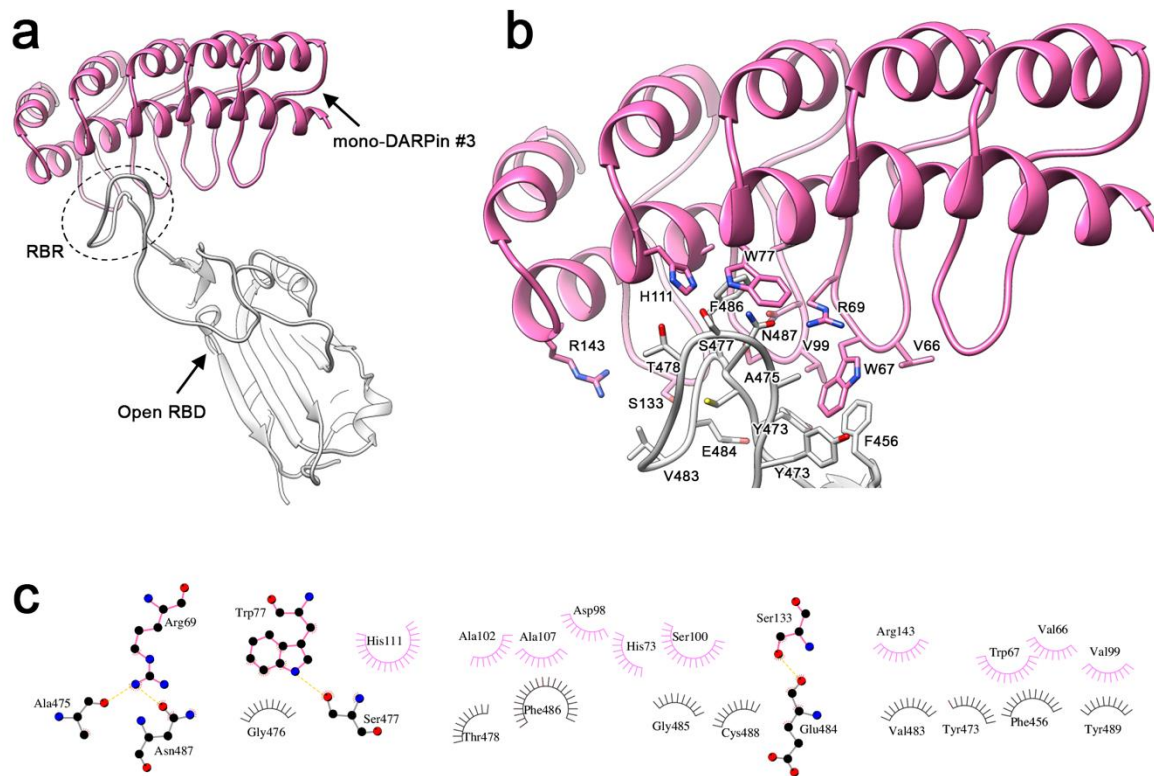
Supplementary Figure 2: Single-particle cryo-EM image processing workflows for each of the mono-DARPin samples.



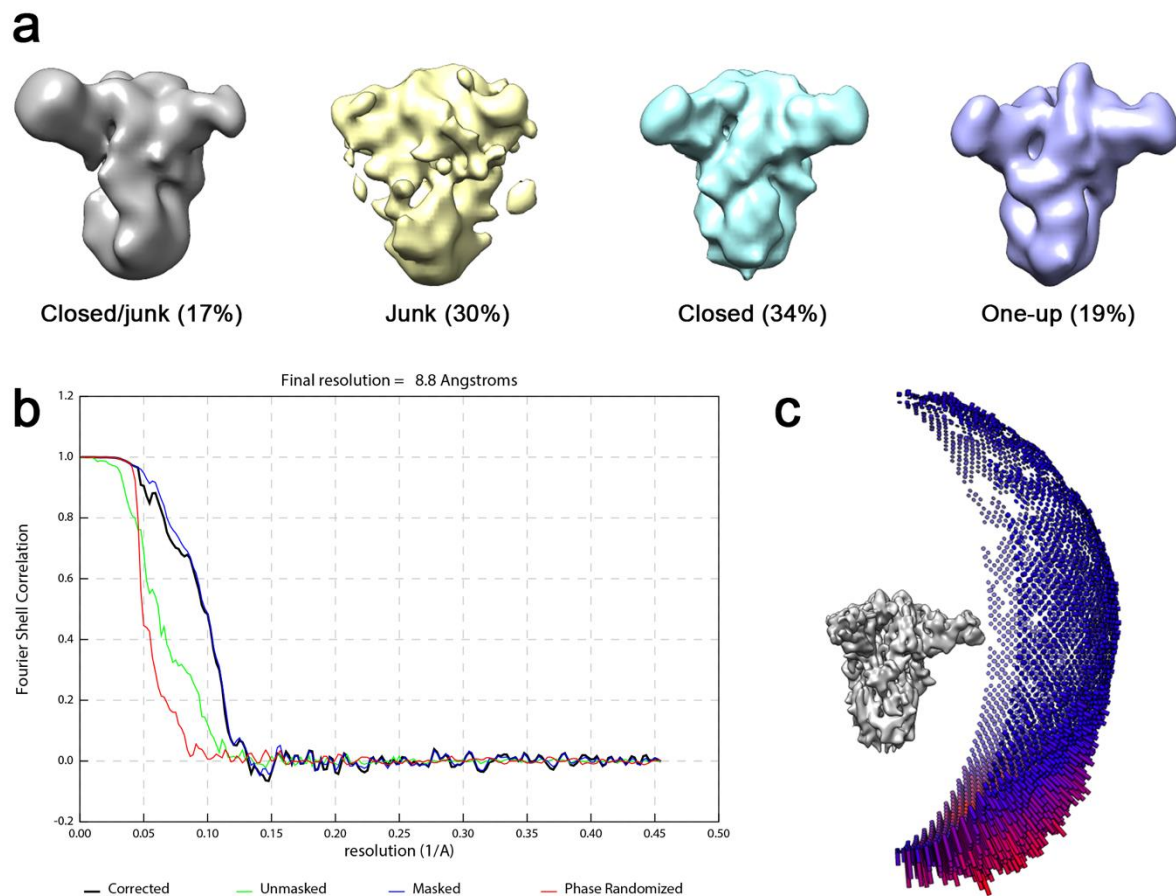
Supplementary Figure 3: a) 3D classes obtained from spike ectodomains incubated with mono-DARPin #3 for 15 seconds, and b) for 60 seconds. c) Gold-standard Fourier shell correlation (FSC) curve generated from the independent half maps contributing to the 6.8 Å resolution density map. d) Angular distribution plot of the final C3 refined EM density map. e) The EM density map of the spike ectodomain bound to three copies of mono-DARPin #3, coloured according to local resolution.



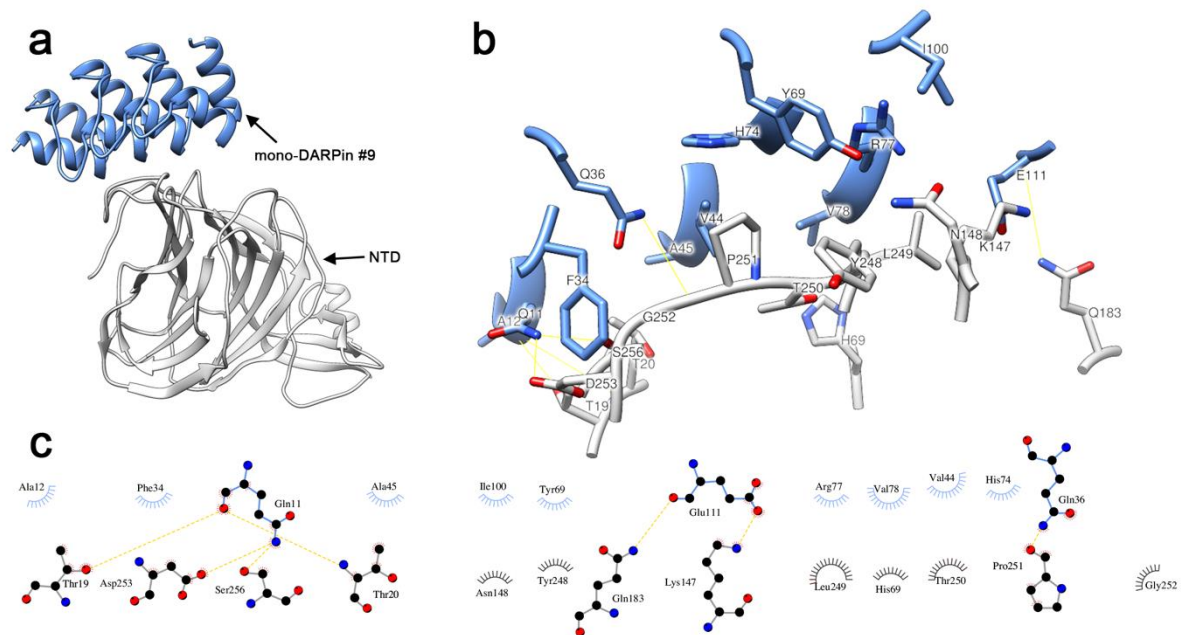
Supplementary Figure 4: a) Cryo-EM density for state 1 and b) state 2 of the SARS-CoV-2 spike ectodomain in complex with the RBD targeting mono-DARPin #3, shown as two orthogonal views. The pseudo-atomic model of mono-DARPin #3 in complex with RBD, derived from molecular docking experiments, is fitted in each of the spike protomers and colored grey and pink, respectively.



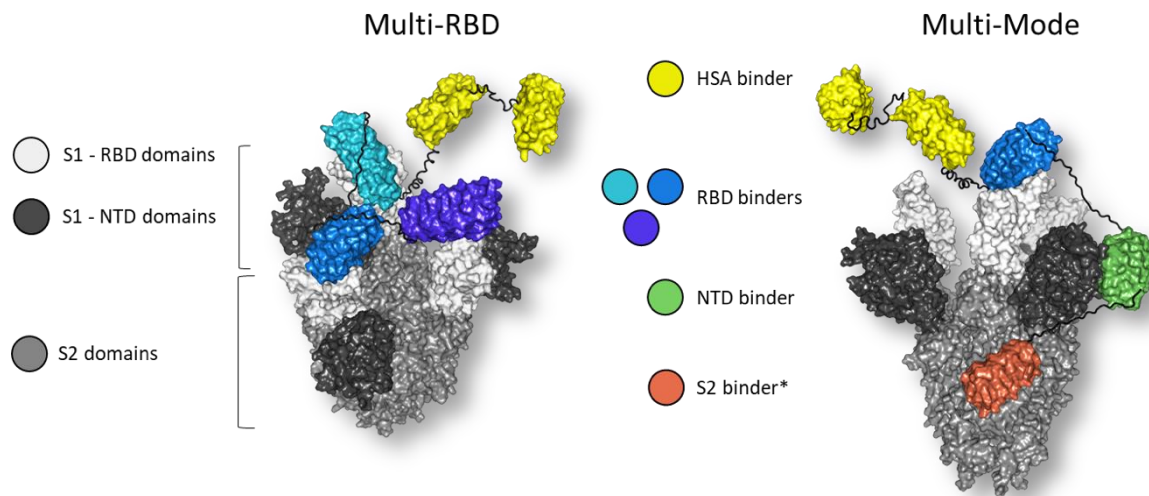
Supplementary Figure 5: a) Pseudo-atomic model of mono-DARPin #3 in complex with the SARS-COV-2 spike RBD colored grey and pink, respectively. b) Zoomed in view of the interface between mono-DARPin #3 and RBD. c) DimPlot(58) representation of putative interacting residues between the spike ectodomain RBD and mono-DARPin #3, identified through molecular docking experiments. Residues participating in hydrophobic interactions are shown as spoke arcs. Residues participating in hydrogen bonding are shown as sticks, and hydrogen bonds are shown as yellow dotted lines. Residues are coloured grey and pink for spike and monoDARPin #3, respectively.



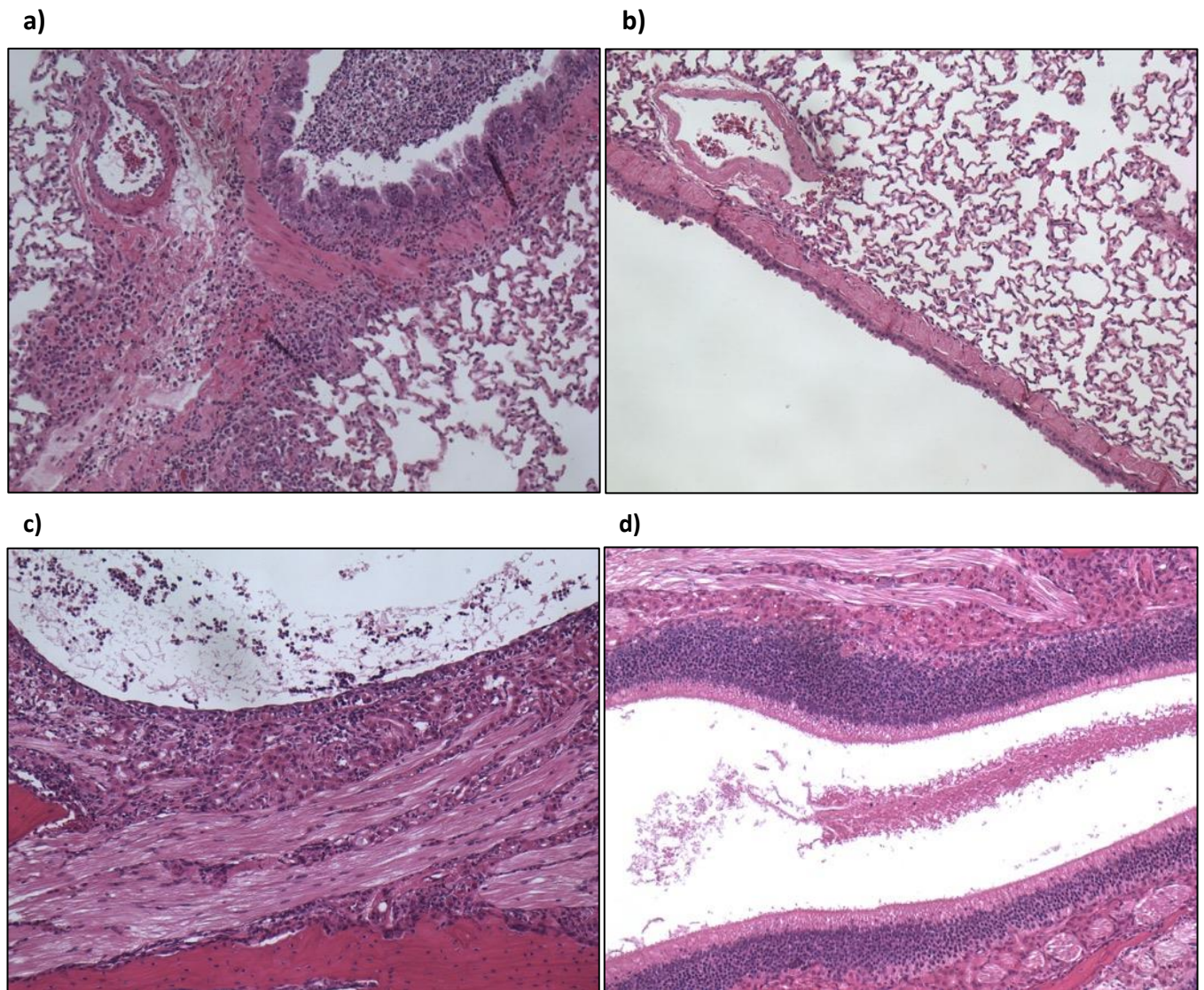
Supplementary Figure 6 a) 3D classes obtained from spike ectodomains incubated with mono-DARPin #9 for 15 seconds. b) Gold-standard Fourier shell correlation (FSC) curve generated from the independent half maps contributing to the 8.8 Å resolution density map. c) Angular distribution plot of the final C3 refined EM density map.



Supplementary Figure 7: a) Pseudo-atomic model of mono-DARPin #9 in complex with the SARS-COV-2 spike NTD colored blue and grey, respectively. b) Zoomed in view of the interface between mono-DARPin #9 and NTD. c) DimPlot(58) representation of putative interacting residues between the spike ectodomain NTD and mono-DARPin #9, identified through molecular docking experiments. Residues participating in hydrophobic interactions are shown as spoke arcs. Residues participating in hydrogen bonding are shown as sticks, and hydrogen bonds are shown as yellow dotted lines. Residues are coloured grey and blue for spike and mono-DARPin #9, respectively.



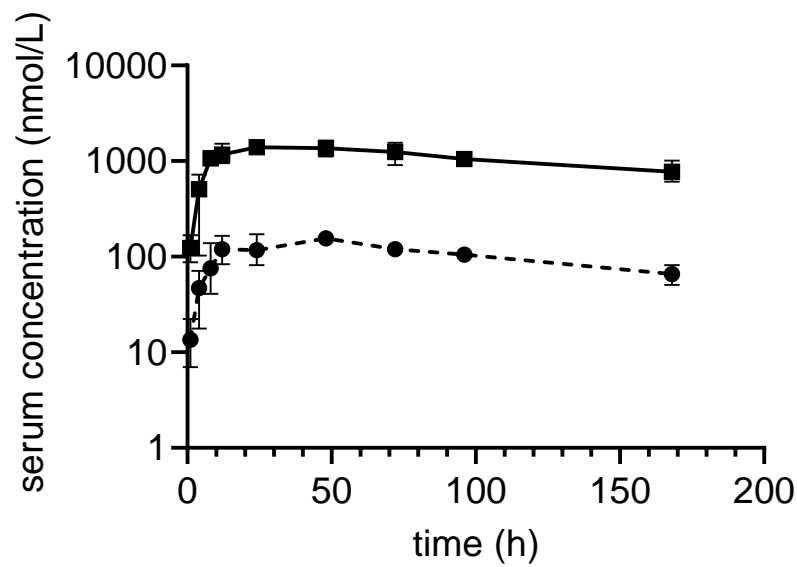
Supplementary Figure 8: Molecular model of multi-DARPin molecule MM-DC (right), consisting of five DARPin domains (yellow: HSA-binding domains, blue: RBD-binding domain, green: NTD-binding domain, orange: S2-binding domain) bound to the spike ectodomain. Linkers are shown in black. Molecular model of MR-DC (left) consisting of five DARPin domains (yellow: HSA-binding domains, shades of blue: RBD-binding domains) bound to the RBDs (white) of the spike ectodomain (grey). Linkers are shown in black. Position of RBD and NTD binders guided by Cryo-EM data (Figure 3) - *Positioning on spike protein remains uncertain for the S2 binder and is guided by manual docking and not based on Cryo-EM data.



Supplementary Figure 9: Representative histopathological microscopic images of lung and nasal turbinates on day 4.

a) Lung from a hamster treated with vehicle: *Moderate mixed inflammatory cell infiltrate (lymphocytes, macrophages, plasma, cells and granulocytes) of the bronchial/bronchiolar epithelium and underlying lamina propria extending to the adjacent blood vessels, alveolar interstitium and spaces with prominent Type II alveolar pneumocytes. Some degeneration, regeneration and disorganization of the bronchial epithelium with single cell necrosis is also evident.* b) Lung from a hamster treated with 1600 ug: *Very minimal mixed inflammatory cell infiltrate (lymphocytes, macrophages, plasma, cells and granulocytes) of the bronchial/bronchiolar epithelium and underlying lamina propria.* c) Nasal turbinates from a hamster treated with vehicle: *A marked mixed inflammatory cell infiltrate (lymphocytes, macrophages, plasma, cells and granulocytes) of the olfactory epithelium with degeneration, regeneration and disorganization of the epithelium, single cell necrosis and inflammatory exudate in the lumen of the nasal cavity.* d) Nasal turbinates from a hamster treated






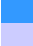
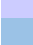

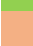

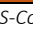
with 1600 ug: *A mild mixed inflammatory cell infiltrate (lymphocytes, macrophages, plasma, cells and granulocytes) of the olfactory epithelium with degeneration, regeneration and disorganization of the epithelium, single cell necrosis and inflammatory exudate in the nasal cavity.*



Supplementary Figure 10: Pharmacokinetic analysis of MR-DC exposure at concentrations of 1 mg/kg (dashed line) and 10 mg/kg (solid line), following i.p. administration. Elimination half-life was calculated to be 4-6 days.

Supplementary Tables

Supplementary Table 1: List of spike protein-binding mono-DARPin molecules and their properties

Name	Binding domain	Viral Neutralization	PsV NA – Screening* [nM]	K_D [nM]	SEC Profile	T_m [°C]	Size [kDa]
1	 RBD	Neutralizing	10	0.258**	Monomer	>65	~14
2	 RBD	Neutralizing	10	0.220***	Monomer	>85	~17
3	 RBD	Neutralizing	10	0.030**	Monomer	>85	~17
4	 RBD	Neutralizing	10	0.390***	Monomer	>85	~17
5	 RBD	Neutralizing	10	0.090**	Monomer	>85	~17
6	 RBD	Neutralizing	10	0.080**	Monomer	>85	~17
7	 RBD	Non-neutralizing	no neutralization	8.10***	Monomer	>80	~14
8	 RBD	Non-neutralizing	no neutralization	10.0***	Monomer	n.a.	~14
9	 NTD	Non-neutralizing	no neutralization	1.24**	Monomer	n.a.	~14
10	 S2	Partial Neutralization	100	0.785**	Monomer	>85	~14
11	 S2	Partial Neutralization	100	n.a.	Monomer	>85	~17

* VSV-SARS-CoV-2 pseudovirus screening assays were performed at 1, 10 and 100nM for all mono-DARPin molecules. The value indicated is the lowest concentration where neutralization or partial neutralization was detected.

** Multi concentration SPR measurement

*** Single concentration SPR measurement

n.a.: not applicable

Supplementary Table 2: Properties of SARS-CoV-2 inhibiting DARPins

Construct Name	5D-Multi-DARPin					IC ₅₀ PsV NA (*Screening Assay 1)	IC ₅₀ PsV NA (*Screening Assay 2)	Live Virus CPE**	SEC Profile	T _m [°C] (CD)
	1	2	3	4	5	[10 ⁻⁹ M]	[10 ⁻⁹ M]	[10 ⁻⁹ M]		
MR-DC	H	H	6	3	5		0.199	0.025	Monomeric	>85
MM-DC	H	H	5	9	10	0.228		0.100	Monomeric	>85
M3	H	H	6	1	3	0.120		0.080	Monomeric	>80
M4	H	H	4	2	1		0.261	0.080	Monomeric	>75
M5	H	H	4	6	3		0.281	n.a	Monomeric	>85
M6	H	H	6	3	6	0.125		0.016	Monomeric	>85
M7	H	H	7	3	6	0.241		0.016	Monomeric	>80
M8	H	H	8	4	1	0.238		0.080	Monomeric	>85
M9	H	H	4	1	8	0.263		0.050	Monomeric	>85
M10	H	H	3	6	9	0.264		0.080	Monomeric	>85
M11	H	H	9	3	6	0.279		0.080	Monomeric	>80
M12	H	H	1	6	9	0.418		0.080	Monomeric	>75
M13	H	H	9	6	1	0.476		0.080	Monomeric	>80
M14	H	H	6	9	10	0.098		0.080	Monomeric	>80
M15	H	H	3	9	11	1.267		0.800	Monomeric	>85
M16	H	H	10	9	6	0.147		0.050	Monomeric	>85
M17	H	H	11	9	3	0.693		n.a	Monomeric	>80
M18	H	H	5	1	3		0.386	n.a	Monomeric	>80
M19	H	H	1	2	5		0.354	0.080	Monomeric	>80
M20	H	H	3	5	6		0.256	0.016	Monomeric	>85
M21	H	H	6	10	11		0.201	0.080	Monomeric	>85
M22	H	H	3	10	10		0.141	0.016	Monomeric	>80

H = Human serum albumin binding DARPins

n.a. = not applicable

* Higher viral titers used during the screening process compared to illustrated titration curves, which results in higher IC₅₀ values

** Titration assays for evaluation of cytopathic effect (CPE) by crystal violet staining. Displayed is the lowest concentration where cell protection was observed.

Supplementary Table 3: Neutralization potency (IC_{50} , [pM]) for multi-DARPin molecules MR-DC and MM-DC for SARS-CoV-2 spike protein variants, frequently observed in sequencing data of globally appearing serotypes, were evaluated by PsV NA.

	wt	G476S	V483A	D614G	D614G x Q675H
MR-DC	16.53	27.08	27.48	11.77	12.11
MM-DC	5.48	14.46	32.40	4.64	22.44

Supplementary Table 4: Cryo-EM data collection and image processing information.

Mono-DARPin (no.)	#3	#3	#3	#9	#10
Magnification	75,000	75,000	92,000	92,000	92,000
Voltage (kV)	300	300	200	200	200
Electron exposure (e-/Å ²)	40	40	40	40	40
Defocus range (μm)	1.25-2.5	1.25-2.5	1.25-2.5	1.25-2.5	1.25-2.5
Pixel size (Å)	1.1	1.1	1.1	1.1	1.1
Symmetry imposed	C3	C1	N/A	C3	N/A
Initial particle images (no.)	123,833	123,833	46,140	16,905	2,705
Final particle images (no.)	53,548	21,612	6,888	8,445	2,090
Map resolution (Å)	6.8	9.6	N/A	8.8	N/A
FSC threshold	0.143	0.143	N/A	0.143	N/A
Map resolution range (Å)	5.5-18.6	8.2-26	N/A	7.1-24.4	N/A

Supplementary Table 5: Overview of fermentation runs performed with anti-SARS-Cov-2 multi-DARPin molecule MP0420 at different scales. Expression yields presented in gram product per liter fermentation broth were determined by SDS-PAGE.

Run	Status	Fermenter Scale	Harvested Amount	Expression Yield
1	Development	5 L	4.9 kg	12.6 g/L
2	Development	5 L	4.9 kg	12.5 g/L
3	Development	5 L	4.9 kg	11.1 g/L
4	GMP	100 L	101 kg	11.3 g/L
5	GMP	100 L	101 kg	12.3 g/L

References

1. P. Zhou *et al.*, A pneumonia outbreak associated with a new coronavirus of probable bat origin. *Nature* **579**, 270-273 (2020).
2. S. Hsiang *et al.*, The effect of large-scale anti-contagion policies on the COVID-19 pandemic. *Nature* **584**, 262-267 (2020).
3. S. Flaxman *et al.*, Estimating the effects of non-pharmaceutical interventions on COVID-19 in Europe. *Nature* **584**, 257-261 (2020).
4. R. K. Guy, R. S. DiPaola, F. Romanelli, R. E. Dutch, Rapid repurposing of drugs for COVID-19. *Science* **368**, 829-830 (2020).
5. H. Ledford, Antibody therapies could be a bridge to a coronavirus vaccine - but will the world benefit? *Nature* **584**, 333-334 (2020).
6. H. K. Binz *et al.*, High-affinity binders selected from designed ankyrin repeat protein libraries. *Nat Biotechnol* **22**, 575-582 (2004).
7. R. D. Baird *et al.*, First-in-Human Phase I Study of MP0250, a First-in-Class DARPIn Drug Candidate Targeting VEGF and HGF, in Patients With Advanced Solid Tumors. *J Clin Oncol* **in press**, (2020).
8. J. Shang *et al.*, Structural basis of receptor recognition by SARS-CoV-2. *Nature* **581**, 221-224 (2020).
9. M. A. Tortorici, D. Veisler, Structural insights into coronavirus entry. *Adv Virus Res* **105**, 93-116 (2019).
10. M. Letko, A. Marzi, V. Munster, Functional assessment of cell entry and receptor usage for SARS-CoV-2 and other lineage B betacoronaviruses. *Nat Microbiol* **5**, 562-569 (2020).
11. M. Hoffmann *et al.*, SARS-CoV-2 Cell Entry Depends on ACE2 and TMPRSS2 and Is Blocked by a Clinically Proven Protease Inhibitor. *Cell* **181**, 271-280 e278 (2020).
12. A. C. Walls *et al.*, Cryo-electron microscopy structure of a coronavirus spike glycoprotein trimer. *Nature* **531**, 114-117 (2016).
13. A. C. Walls *et al.*, Structure, Function, and Antigenicity of the SARS-CoV-2 Spike Glycoprotein. *Cell* **181**, 281-292 e286 (2020).
14. A. C. Walls *et al.*, Tectonic conformational changes of a coronavirus spike glycoprotein promote membrane fusion. *Proc Natl Acad Sci U S A* **114**, 11157-11162 (2017).
15. C. Zahnd, P. Amstutz, A. Pluckthun, Ribosome display: selecting and evolving proteins in vitro that specifically bind to a target. *Nat Methods* **4**, 269-279 (2007).
16. J. Hanes, L. Jermutus, S. Weber-Bornhauser, H. R. Bosshard, A. Pluckthun, Ribosome display efficiently selects and evolves high-affinity antibodies in vitro from immune libraries. *Proc Natl Acad Sci U S A* **95**, 14130-14135 (1998).
17. H. K. Binz, M. T. Stumpp, P. Forrer, P. Amstutz, A. Pluckthun, Designing repeat proteins: well-expressed, soluble and stable proteins from combinatorial libraries of consensus ankyrin repeat proteins. *J Mol Biol* **332**, 489-503 (2003).
18. A. C. Walls *et al.*, Unexpected Receptor Functional Mimicry Elucidates Activation of Coronavirus Fusion. *Cell* **176**, 1026-1039 e1015 (2019).
19. F. H. Niesen, H. Berglund, M. Vedadi, The use of differential scanning fluorimetry to detect ligand interactions that promote protein stability. *Nat Protoc* **2**, 2212-2221 (2007).
20. J. Hansen *et al.*, Studies in humanized mice and convalescent humans yield a SARS-CoV-2 antibody cocktail. *Science*, (2020).

21. D. Pinto *et al.*, Cross-neutralization of SARS-CoV-2 by a human monoclonal SARS-CoV antibody. *Nature* **583**, 290-295 (2020).
22. C. O. Barnes *et al.*, Structures of Human Antibodies Bound to SARS-CoV-2 Spike Reveal Common Epitopes and Recurrent Features of Antibodies. *Cell*, (2020).
23. D. Wrapp *et al.*, Cryo-EM structure of the 2019-nCoV spike in the prefusion conformation. *Science* **367**, 1260-1263 (2020).
24. Wrobel, SARS-CoV-2 and bat RaTG13 spike glycoprotein structures inform on virus evolution and furin-cleavage effects. (2020).
25. Y. Cai, Distinct conformational states of SARS-CoV-2 spike protein. (2020).
26. X. Chi *et al.*, A neutralizing human antibody binds to the N-terminal domain of the Spike protein of SARS-CoV-2. *Science* **369**, 650-655 (2020).
27. A. Baum *et al.*, REGN-COV2 antibodies prevent and treat SARS-CoV-2 infection in rhesus macaques and hamsters. *Science*, (2020).
28. P. Chen *et al.*, SARS-CoV-2 Neutralizing Antibody LY-CoV555 in Outpatients with Covid-19. *N Engl J Med*, (2020).
29. B. E. Jones *et al.*, LY-CoV555, a rapidly isolated potent neutralizing antibody, provides protection in a non-human primate model of SARS-CoV-2 infection. *bioRxiv*, (2020).
30. M. T. Stumpp, K. M. Dawson, H. K. Binz, Beyond Antibodies: The DARPIn((R)) Drug Platform. *BioDrugs* **34**, 423-433 (2020).
31. M. Schoof *et al.*, An ultrapotent synthetic nanobody neutralizes SARS-CoV-2 by stabilizing inactive Spike. *Science*, (2020).
32. L. Cao *et al.*, De novo design of picomolar SARS-CoV-2 miniprotein inhibitors. *Science* **370**, 426-431 (2020).
33. T. W. Linsky *et al.*, De novo design of potent and resilient hACE2 decoys to neutralize SARS-CoV-2. *Science*, (2020).
34. J. D. Walter, C. A. J. Hutter, A. A. Garaeva, M. Scherer, I. Zimmermann, Highly potent bispecific sybodies neutralize SARS-CoV-2. *bioRxiv*, (2020).
35. P. J. M. Brouwer *et al.*, Potent neutralizing antibodies from COVID-19 patients define multiple targets of vulnerability. *Science* **369**, 643-650 (2020).
36. L. Liu *et al.*, Potent neutralizing antibodies against multiple epitopes on SARS-CoV-2 spike. *Nature* **584**, 450-456 (2020).
37. T. F. Rogers *et al.*, Isolation of potent SARS-CoV-2 neutralizing antibodies and protection from disease in a small animal model. *Science*, (2020).
38. R. Shi *et al.*, A human neutralizing antibody targets the receptor-binding site of SARS-CoV-2. *Nature* **584**, 120-124 (2020).
39. S. J. Zost *et al.*, Potently neutralizing and protective human antibodies against SARS-CoV-2. *Nature* **584**, 443-449 (2020).
40. L. Liu *et al.*, Anti-spike IgG causes severe acute lung injury by skewing macrophage responses during acute SARS-CoV infection. *JCI Insight* **4**, (2019).
41. A. M. Arvin *et al.*, A perspective on potential antibody-dependent enhancement of SARS-CoV-2. *Nature* **584**, 353-363 (2020).
42. A. Renn, Y. Fu, X. Hu, M. D. Hall, A. Simeonov, Fruitful Neutralizing Antibody Pipeline Brings Hope To Defeat SARS-Cov-2. *Trends Pharmacol Sci* **41**, 815-829 (2020).
43. T. Zohar, G. Alter, Dissecting antibody-mediated protection against SARS-CoV-2. *Nat Rev Immunol* **20**, 392-394 (2020).
44. H. Ledford, The race to make COVID antibody therapies cheaper and more potent. *Nature* **587**, 18 (2020).

45. H. K. Binz *et al.*, Design and characterization of MP0250, a tri-specific anti-HGF/anti-VEGF DARPIn(R) drug candidate. *MAbs* **9**, 1262-1269 (2017).
46. G. Torriani *et al.*, Macropinocytosis contributes to hantavirus entry into human airway epithelial cells. *Virology* **531**, 57-68 (2019).
47. C. Wang *et al.*, A human monoclonal antibody blocking SARS-CoV-2 infection. *Nat Commun* **11**, 2251 (2020).
48. J. Zivanov *et al.*, New tools for automated high-resolution cryo-EM structure determination in RELION-3. *Elife* **7**, (2018).
49. S. Q. Zheng *et al.*, MotionCor2: anisotropic correction of beam-induced motion for improved cryo-electron microscopy. *Nat Methods* **14**, 331-332 (2017).
50. K. Zhang, Gctf: Real-time CTF determination and correction. *J Struct Biol* **193**, 1-12 (2016).
51. A. Leaver-Fay *et al.*, ROSETTA3: an object-oriented software suite for the simulation and design of macromolecules. *Methods Enzymol* **487**, 545-574 (2011).
52. P. S. Huang *et al.*, RosettaRemodel: a generalized framework for flexible backbone protein design. *PLoS One* **6**, e24109 (2011).
53. L. G. Nivon, R. Moretti, D. Baker, A Pareto-optimal refinement method for protein design scaffolds. *PLoS One* **8**, e59004 (2013).
54. D. L. Hurdiss *et al.*, Cryo-EM structure of coronavirus-HKU1 haemagglutinin esterase reveals architectural changes arising from prolonged circulation in humans. *Nat Commun* **11**, 4646 (2020).
55. S. Chaudhury *et al.*, Benchmarking and analysis of protein docking performance in Rosetta v3.2. *PLoS One* **6**, e22477 (2011).
56. A. C. Wallace, R. A. Laskowski, J. M. Thornton, LIGPLOT: a program to generate schematic diagrams of protein-ligand interactions. *Protein Eng* **8**, 127-134 (1995).
57. E. F. Pettersen *et al.*, UCSF Chimera--a visualization system for exploratory research and analysis. *J Comput Chem* **25**, 1605-1612 (2004).
58. R. A. Laskowski, M. B. Swindells, LigPlot+: multiple ligand-protein interaction diagrams for drug discovery. *J Chem Inf Model* **51**, 2778-2786 (2011).